Ab initio Description of Materials Properties: An Application to Thermoelectric and Raman Scattering Phenomena.

JUSTUS-LIEBIG-
UNIVERSITÄT
GIESSEN

DISSERTATION

submitted for the degree of

Doctor rerum naturalium
(*Dr. rer. nat.*)

by
M. Sc. Juan Manuel GUERRA-CASTRO

Supervisor: Prof. Dr. Christian Heiliger
AG Theoretische Festkörperphysik

Institut für Theoretische Physik
Justus-Liebig-Universität Gießen

Gießen, April 2019

Dedico este trabajo a mi familia y amigos.
(I dedicate this work to my family and friends)

Contents

Contents

4

1 Introduction

Nowadays, an intense research effort is devoted to the field of materials science - as a converging point between physics and chemistry - to develop and understand new sustainable alternatives to raw materials for industrial applications and environmental preservation. The rapidly growing of human population leads to a higher energy demand thus requiring new scientific strategies to replace or at least supplement conventional power production - such as nuclear power or hydroelectric plants - by alternative technologies like thermoelectric generators or solar panels.

This is the main objective of the *Research Training Group* (RTG) 2204 "substitute materials for sustainable energy technologies", affiliated to the Center for Materials Research (LAMA), at the University of Giessen. The focus of the RTG2204 is the study of highly specialized and abundant functional materials aimed at a massive production of renewable energy technologies. The team is composed by scientists of twelve research groups belonging to six institutes and studying in the following fields: Thermoelectric generators, high-efficiency photovoltaics, large-scale rechargeable batteries, intelligent glazing, and carbon-based technologies for energy-efficient applications. The collaboration between the scientists is aimed to provide technologies for production, development, characterization and recycling of raw materials.

The research facilities at each institute allow the measurement of different materials properties, such as thermoelectric transport, photovoltaic responses and general optical properties, mechanical properties, and so forth. The overall research is mostly done by experimental scientists, but the collaborative work between researchers yields the possibility of a simultaneous measurement and simulation of the physical situations. Hence, the participation of researchers in the area of computational and theoretical sciences is fundamental for a more complete understanding of all phenomena in materials science.

New discoveries in materials science come from different sources. As an example, an exhaustive exploration of the periodic table of elements, and their *unbounded* possibility of combinations, have yielded groundbreaking achievements in this field but under practical and heuristic algorithms: the search of new materials with particular properties, e.g.,

optimal thermoelectric performance, etc. nano-structuring, as another example, or exploiting atomic-like properties, requires big scientific efforts in order to control the physical parameters at these scales. In this way, it is possible to observe transport in few-electron systems, confinement and quantum effects. The limitations arise when a massive and large-scale production of atomic-like devices is needed. There, simulations play an important role in the prediction of possible outcomes since they base in fundamental laws and the satisfactory agreement with experiments.

As a first step in the process of discovery, one has to track back the state-of-the-art of the most promising materials, if already existing, to evaluate alternatives for their optimization or substitution, production costs, and environmental impact. As treated in this thesis, silicon (Si) is regarded as one of the most abundant materials in the earth crust and is nearly 100% recyclable. However, its relatively low efficiency in thermoelectrics limits its technological application as a thermoelectric device and demands its substitution by, for instance, the iso-electronic germanium (Ge) that shows a better performance. However, the costs of production are much higher than that of Si and its not optimally recycled. There are plenty of examples in materials science in which there is a competition between a material's efficiency, in some particular parameter, and its toxicity or scarcity. One important branch in modern materials research deals with the optimization of material properties under some constrictions, for instance, thermoelectric performance vs. production costs. Another alternative is to explore the theoretical potential energy landscapes for the formation of binary compounds. However, the possible combinations are huge and impractical. Therefore, the search is always bounded, e.g., by physical reasoning.

Many practical problems in the world are being tackled by materials science, specially those related to energy conversion/storage and alternatives to fuel and energy consumption. Abundant materials like hydrogen are subject of intense research to mitigate the demand of global energy consumption since these materials can be activated by the sun light and therefore are clean sources of energy.

It is therefore mandatory to devote the research to the practical and, at the same time, fundamental problems involving the preservation of nature, environment, at individual and industrial scale. My role as a Ph. D. candidate of the RTG 2204 is to support and provide computational simulations to material systems to interpret their results and to predict situations not yet accessible in experiments. The basis of the simulations goes back to the discovery of quantum mechanics and its application to solids: theoretical solid state physics, or condensed matter physics.

The main focus on this approach corresponds to *ab initio* - density functional theory - methods. Computational sciences have grown in parallel and nowadays there are plenty, but not infinite, of tools that allow to concentrate in the solution of particular problems rather than in the details of the programming language. Also, the diversity in the formalism offers the possibility of modeling different physical situations and to explore intrinsic and probably unexplored materials properties.

During the course of this doctoral training, I have attended different seminars about environmental management, recycling strategies and physical sciences. Therefore, I regard this experience as an introduction to the scientific community and as a skilled preparation for the job market. From the *ambitious* point of view of theoretical solid state physics, all experiments covered within the research groups affiliated to LAMA and RTG2204 are sensible to be simulated and explained from the theory grounds, but unfortunately time is always a realistic boundary. Therefore, despite my desire of getting involved in all the projects, I will present below the results of my participation in only a very few, but substantial, collection of these projects.

I want to mention that the structure of this thesis corresponds to a logical order, rather than a historical order, because it has been developed from intuition, intensive research and detailed discussions with researchers in different contexts. It was, of course, written after an intensive review of the theoretical background and the state of the art of the projects.

Firstly, I addressed the topic of electronic properties of thermoelectric Mg_2X systems. Using elemental solid state physics, I tried to cover all crystalline properties of these materials and intermediate alloys. These properties are the formation energies to account for stability, the mapping of electronic band structures for intermediate compounds, energy band gaps, effective masses, and the issues related to the theoretical limitations. In order to define this problem, since there are still plenty of open questions about the functionality of these materials, I concentrated on the physical observables that can be extracted from the electronic properties obtained from the DFT methods developed in the AG Heiliger, i.e., the Green's functions KKR formalism. I figured out that this is a nowadays interesting research topic since there are many physical properties not yet reported and not even understood.

Similarly, as is also in the research scope of the AG Heiliger, I decided to address the problem of Raman spectroscopy in graphene from first-principle calculations. As a first approximation, the equilibrium and zero absolute temperature properties provide a very good description of this phenomenon since no phase transitions or thermal effects are

directly involved. Then, using bare conservation rules, I developed a phenomenological approach that satisfactorily accounted for the observed Raman shifts induced by the excitation laser energy used and micro-crystalline effects of the sample. This approach allowed me to understand and explain many observed properties. However, some others are still not accessible from the description. It is my intention with this approach to open a venue to a more complete description of the Raman phenomena in micro-crystalline samples that can in principle be complemented with the experience of the research group in this field.

2 Theoretical Foundations

In this section I present an introduction to the theoretical techniques required to describe the electronic and structural properties of the material systems. These systems can be either symmetric pristine crystals as well as materials with defects. The latter comprises different categories, such as point defects as in-site alloy substitutions, or extended defects such as boundaries in the materials.

Therefore, I exploit the fact that quantum mechanics predicts with a very good accuracy the material's observables at the atomic scale and, thus, all macroscopic quantities. However, a direct solution of the complex many-body problem is not always possible and in most practical cases completely unknown. Fortunately, a detailed analytic solution to such a problem is not always needed since there are different ways to approximate this problem. All approximations rely on some basic assumptions, such as that the single-electron is embedded in an effective medium that self-consistently reaches its equilibrium in the ground state of the system.

First, I will review the basics of density functional theory (DFT) from a practical point of view, without a rigorous mathematical treatment but rather taking advantage of the vast existing literature and computational algorithms based on this formalism. As part of the approximate solutions to the quantum mechanical laws, i.e., the Schrödinger's equation, I will review the Green's functions (GF) formalism as part of the multiple-scattering theory. Within this theory, the Korringa-Kohn and Rostocker (KKR) method plays an important role since it provides a set of relatively simplified formulas to compute the band structure of materials, based on a spherical expansion of the background potentials.

To treat alloy systems there are several alternatives at present, such as supercells, virtual crystal approximations, and the coherent potential approximation (CPA). In the language of the multiple-scattering theory, the CPA allows to define an effective single-site scattering potential that solves self-consistently the system's GF and therefore all physical quantities of the system can be obtained by means of the Bloch spectral density function (BSF).

Finally, for the sake of completeness in the study of materials, the

phonon dynamics must be included and their contributions to the total free energy. By means of a convenient separation of the Schrödinger's equation, the Born-Oppenheimer approximation, the electronic and phonon dynamics are decoupled and then treated using linear response perturbation theory. These calculations are essential to model many properties of the materials, especially those dependent on temperature or the material response to external electromagnetic fields.

2.1 Introduction to Density Functional Theory

DFT represents an alternative to electronic structure calculations in which the electronic density of states (DOS) $n(\mathbf{r})$, rather than the many-electron wave function, is the main actor.[1] Any problem in the electronic structure of matter is solved by the Schrödinger equation including the time.[2] In general, a material system can be described as a collection of interacting atoms under the influence of some external fields.[3] This system may be in either the gas phase, such as molecules, clusters, etc., or in a solid phase, such as bulk materials, surfaces, etc. At this scale, the materials are described as a set of electrons and atomic nuclei interacting via Coulomb electrostatic forces with a modeling Hamiltonian such as

$$
\hat{H} = -\underbrace{\sum_{i=1}^{N} \frac{\hbar^2}{2m}\nabla_i^2}_{\hat{T}} - \underbrace{\sum_{I=1}^{P} \frac{\hbar^2}{2M_I}\nabla_I^2}_{\hat{T}_n} + \underbrace{\frac{e^2}{2}\sum_{i=1}^{N}\sum_{j\neq i}^{N} \frac{1}{|\mathbf{r}_i - \mathbf{r}_j|}}_{\hat{V}_{ee}}
$$

$$
+ \underbrace{\frac{e^2}{2}\sum_{I=1}^{P}\sum_{J\neq I}^{P} \frac{Z_I Z_J}{|\mathbf{R}_I - \mathbf{R}_J|}}_{\hat{V}_{nn}} - \underbrace{e^2\sum_{i=1}^{N}\sum_{I=1}^{P} \frac{Z_I}{|\mathbf{r}_i - \mathbf{R}_I|}}_{\hat{V}_{en}}. \quad (2.1)
$$

Here, $\mathbf{r} = \{\mathbf{r}_i, i = 1, ..., N\}$ is a set of N electronic coordinates, and $\mathbf{R} = \{\mathbf{R}_I, I = 1, ..., P\}$ is a set of P nuclear coordinates, and Z_I and M_I are the nuclear charge and masses, respectively. In this equation, $\hat{T}$ represents the (non-local) electronic kinetic operator, $\hat{T}_n$ is the nuclear kinetic operator, $\hat{V}_{ee}$ represents the electron-electron interaction operator, $\hat{V}_{nn}$ is the nuclear-nuclear operator, and $\hat{V}_{en}$ represents the electron-nuclear interaction.

The nature of electrons is fermionic, and therefore the total wave function must preserve its nature and be antisymmetric under the exchange

of the coordinates of an indistinguishable electron pair. Different nuclear species may be distinguishable and they may obey either Fermi statistics, for half-integer nuclear spin, or Bose-Einstein statistics for integer nuclear spin. In principle, all the properties can be derived by solving the time-independent Schrödinger equation:

$$\hat{H}\psi_n(\mathbf{r}, \mathbf{R}) = \varepsilon_n \psi_n(\mathbf{r}, \mathbf{R}), \tag{2.2}$$

where ε_n are the eigenenergies and $\psi_n(\mathbf{r}, \mathbf{R})$ are the corresponding antisymmetric eigenstates, or wave-functions. This equation, eq. (2.2), is practically impossible to solve analytically. An exact solution exists for a few limited cases, such as the hydrogen-like atoms and related di-molecules. This difficulty arises, most importantly, from the fact that in this many-body system the nature of the two-body Coulomb interaction precludes this equation to be separable. An attempt to make it separable is known as the *Born-Oppenheimer* approximation or *adiabatic* approximation; they proposed a scheme for separating the motion of the nuclei from that of the electrons. This approximation represents an alternative solution to solve eq. (2.2) of the form

$$\psi_n(\mathbf{r}, \mathbf{R}, t) = \sum_n \Theta_n(\mathbf{R}, t)\Phi_n(\mathbf{r}, \mathbf{R}), \tag{2.3}$$

where $\Theta_n(\mathbf{R}, t)$ are wave functions describing the time-evolution of the nuclear subsystem in each of the adiabatic electronic eigenstates $\Phi_n(\mathbf{r}, \mathbf{R})$. These eigenstates satisfy the time-independent Schrödinger equation

$$\hat{h}_e\Phi_n(\mathbf{r}, \mathbf{R}) = E_n\Phi_n(\mathbf{r}, \mathbf{R}), \tag{2.4}$$

where the electronic Hamiltonian, in accordance to that presented in eq. (2.1), is given by

$$\hat{h}_e = \hat{T} + \hat{H}_{ee} + \hat{V}_{ne} = \hat{H} - \hat{T}_n - \hat{V}_{nn}. \tag{2.5}$$

In this partial differential equation on the $\mathbf{r}$ variables, the $3P$ nuclear coordinates $\mathbf{R}$ enter as parameters. The key issue for studying and analyzing the structure of matter is, therefore, to solve the electronic Schrödinger equation $\hat{h}\Psi(\mathbf{r}, \mathbf{R}) = \varepsilon(\mathbf{R})\Psi(\mathbf{r}, \mathbf{R})$ for a system of N interacting electrons in the external Coulomb field generated by a collection of atomic nuclei. The eigenenergies also depend parametrically on $\mathbf{R}$, and define the different potential landscapes.

The first approach to the many-electron problem may be considered to be the one proposed by Hartree in 1928. The basic assumption is that the many-electron wave function, $\Psi(\mathbf{r}, \mathbf{R})$, can be written as a simple product of *one-electron* orbitals, $\varphi_n(\mathbf{r}, \mathbf{R})$. He introduced the *self-consistent field* (SCF) approach in a qualitative way. After that, Slater in 1928 put this method into a mathematical background, by formulating a total wave function of the product form

$$\Phi(\mathbf{r}) = \prod_{i=1}^{N} \varphi_i(\mathbf{r}_i). \tag{2.6}$$

Within this approximation, the total energy is found self-consistently using an ansatz wave function, eq. (2.6), and then perform variations with respect to the one-electron orbitals φ_i. Within this approximation, one can apply a variational principle under the normalization of the individual orbital wave functions, φ_i, and using the eigenenergies as Lagrange multipliers.

The Lagrange equations lead to an effective Schrödinger equation of the form,

$$\left(-\frac{\hbar^2}{2m} \nabla^2 + v_{eff}^{(i)}(\mathbf{r}, \mathbf{R}) \right) \varphi_i(\mathbf{r}) = \varepsilon_i \varphi_i(\mathbf{r}) \tag{2.7}$$

with

$$v_{eff}^{(i)}(\mathbf{r}, \mathbf{R}) = v_{ext}(\mathbf{r}, \mathbf{R}) + \int \frac{\sum_{j \neq i}^{N} |\varphi_j(\mathbf{r}')|^2}{|\mathbf{r} - \mathbf{r}'|} d\mathbf{r}'. \tag{2.8}$$

This approach does not contain the Fermi nature of the electrons and assume them as distinguishable particles. Pauli's principle can be introduced using an antisymmetrized many-electron wave function in the form of a Slater determinant in the single-electronic spin orbital wave functions. This wave function introduces particle exchange in the Hartree-Fock approximation. Within this approximation, the Coulomb many-body correlations between electrons are absent but yields a reasonable good description of atomic bonding. The eq. (2.7) and eq. (2.8) are called the SCF Hartree equations.

In 1927-1928,[4,5] Thomas and Fermi proposed the full electronic density $n(\mathbf{r})$ as the fundamental variable of the many-body problem, that settles down the basis for the latter development of *density functional theory*, or DFT. They proposed an expression for the total electronic energy, obtained through eq. (2.5), where the individual components are

taken from the homogeneous electron gas. The construction of these quantities for an inhomogeneous system follows the integral-functional formula,

$$E_\alpha[\rho] = \int \rho(\mathbf{r})\varepsilon_\alpha[\rho(\mathbf{r})]d\mathbf{r}, \tag{2.9}$$

where the subscript α stands for the kinetic, exchange, and correlation contributions to the total electronic energy. Using this notation, the energy terms are assumed to be functionals of the charge density calculated locally at every point in space. This was the first time that the *local density approximation* (LDA) was proposed. The density of an electron gas is known and given, and therefore the kinetic energy as functional of it. The LDA kinetic energy is

$$T_{TF} = C_k \int \rho(\mathbf{r})^{5/3}d\mathbf{r}, \tag{2.10}$$

with $C_k = 3(3\pi^2)^{2/3}/10(= 2.871)$ Hartree is the atomic unit of energy equivalent to twice the ionization energy of the hydrogen atom (27.21 eV). Exchange can also be introduced by considering Slater's expression for the homogeneous electron gas, as it was done by Dirac in 1930 and Slater in 1951,[6,7]

$$E_X[\rho] = -C_X \int \rho(\mathbf{r})^{4/3}d\mathbf{r}, \tag{2.11}$$

with $C_X[\rho] = 3(3/\pi)^{1/3}/4(= 0.739)$ Hartree, in the so called *Thomas-Fermi-Dirac* approximation. Correlation can also be included even for a local approximation to the homogeneous electron gas, to obtain an energy functional of the electronic variables exclusively through its density. Any component of the energy functional $E[\rho]$, is minimized by the density $\rho(\mathbf{r})$ by means of some variational principle, subject to the constraint that the total integrated charge is equal to the total number of electrons, i.e., $\int \rho(\mathbf{r})d\mathbf{r} = N$. The research effort has shown that the LDA, and its extension to systems with unpaired spin, gives ionization energies of atoms, dissociation energies of molecules and cohesive energies with a fair accuracy of typically $10 - 20\%$. However the LDA gives bond lengths and thus the geometries of molecules and solids typically with a very good accuracy of $\sim 1\%$.[1]

In 1964,[8] Hohenberg and Kohn formulated and proved a theorem that put the former ideas on solid mathematical grounds. They describe the

unique relationship between the total energy of a system of electrons moving under the influence of an external potential and the charge density. Their theorems state that the total energy and thus the external potential are both a unique functional of the electronic density, i.e., $E = E[n(\mathbf{r})]$ and $v_{ext}[n(\mathbf{r})]$. The energy functional can be written in the following way:

$$E[n(\mathbf{r})] = \int n(\mathbf{r})v_{ext}[n(\mathbf{r})]d\mathbf{r} + F[n(\mathbf{r})], \qquad (2.12)$$

where $F[n(\mathbf{r})]$ is an unknown potential functional that depends only upon the density $n(\mathbf{r})$. The second theorem states that the ground state energy can be obtained variationally: the density that minimizes the total energy is the exact ground state density. As a collorary, *since $\rho(\mathbf{r})$ univocally determines $v_{ext}(\mathbf{r})$, it also determines the many-body ground state wave function Φ, which should be obtained by solving the full many-body Schrödinger equation.*

Then, in 1982,[9] Levy reformulated this theory in order to include the antisymmetric nature of the density arising from the antisymmetric wave functions. Kohn and Sham in 1965 presented a practical scheme for determining the ground state properties and generalizations for the excited states.[10]

In this approach, one can self-consistently find the energy solutions of the system using a trial wave function as an initial guess. Note that the Hartree contribution to the electron-electron interaction energy can, in principle, be solved exactly by using classical electrodynamics. The exchange energy can also be solved exactly, and therefore the most difficult term will be the correlation energy.

The Kohn and Sham approach is based on an energy functional, expressed in terms of the occupied orbitals, that minimize the non-interacting electronic kinetic energy under a fixed density constraint. Besides the great success of this approximation, the physical meaning of the quantities involved, the Kohn-Sham orbitals and the eigenenergies, is still under an intense debate.[3] Kohn and Sham provide a self-consistent scheme to find the DOS of the system from a reference potential. They also extend this theory to spin-polarized systems.

Therefore, the strategy to attack the many-body electronic problem is to divide the total energy of an electronic system, given by eq. (2.5), into a number of different contributions, $E[\rho] = T + v_{ext} + E_H + E_X + \overline{E}_C$, each of which can be addressed separately. The decomposed factors come from the operator $\hat{H}_{ee}$ and correspond to the classical electron-electron interaction or Hartree term (E_H), the exchange energy (E_X), and the

coupling constant averaged correlation term ($\overline{E}_C$).

The big issue here is the correlation energy. One of the natural starting point is the homogeneous electron gas. Besides the Dirac approximation, excellent approximations are also available, e.g., due to von Barth and Hedin,[11] Vosko et al,[12] Perdew and Zunger,[13] and Ceperley and Alder using quantum Monte Carlo simulations.[14]

In the local density approximation (LDA), the main idea is to consider a general inhomogeneous electronic system as locally homogeneous, and then to use the exchange-correlation hole corresponding to the homogeneous electron gas.

More generally, gradient expansions address the problem of inhomogeneities in the electronic density using an expansion of the density in terms of gradient and higher derivatives in space. In general, the exchange-correlation energy can be written in the following form:

$$E_{XC}[\rho] = \int \rho(\mathbf{r})\varepsilon_{XC}[\rho(\mathbf{r})]F_{XC}[\rho(\mathbf{r}), \nabla\rho(\mathbf{r}), \nabla^2\rho(\mathbf{r}), ...]d\mathbf{r} \quad (2.13)$$

The second order expansion of this equation corresponds to the *generalized gradient approximation* (GGA) which is valid for densities that vary slowly in space. Among the most common functionals, there exist the Langreth-Mehl functional,[15] Becke-BLYP,[16] Perdew, Burke, and Ernzerhof (PBE) and revisions,[17] and finally the meta-generalized and hybrid functionals.[1]

The practical usability of ground-state DFT to describe physical properties depends entirely on whether approximations for the functional $E_{XC}[n(\mathbf{r})]$ can be done which are simple and sufficiently accurate for the particular physical system. There are, as well, some hybrid methods, like $E_{xc}^{hyb} = \alpha E_x^{KS} + (1 - \alpha)E_{xc}^{GGA}$.[1]

In the Kohn-Sham formulation of DFT, as a generalization of the Hartree-Fock SCF theory given by eq. (2.7) and eq. (2.8), deals with the solution of the eigenvalue equation:

$$\left\{ -\frac{\hbar^2}{2m}\nabla^2 + v_{ext}(\mathbf{r}) + \int \frac{\rho(\mathbf{r}')}{|\mathbf{r} - \mathbf{r}'|}d\mathbf{r}' + \mu_{XC}[\rho] \right\} \varphi_i(\mathbf{r}) = \varepsilon_i\varphi_i(\mathbf{r}), \quad (2.14)$$

where the electron density is given by

$$\rho(\mathbf{r}) = \sum_{i=1}^{N} f_i |\varphi_i(\mathbf{r})|^2. \quad (2.15)$$

In these equations, N represents the number of electrons, and f_i are the occupation numbers corresponding to the one-electron eigenstates; in the case of spin-unpolarized insulators or closed shell molecules, $f_i = 2$ for the $N/2$ lowest eigenstates and $f_i = 0$ otherwise. For spin-polarized and open shell molecules the exchange-correlation and external (whether magnetic or not) potentials depend on the spin projection. The same situation happens when the spin-orbit coupling is considered.

In the electron-nuclear interaction, it is customary to distinguish between the *valence electrons*, that contribute to chemical bonding, and the tightly bound *core electrons* which do not participate in bonding; although this is only a way of labeling without general validity.

In that case, it is possible to reduce the electronic degrees of freedom by replacing the atomic nuclei with a still point-like - effective - nucleus of charge $Z_V = Z - Z_{core}$, with Z_{core} the charge associated with the core electrons.

In solid state physics, the periodicity defines an infinite crystal by repeating the elemental *unit* or *Wigner-Seitz* cell. The *unit* vectors reproduce the infinite solid and are in general non-orthogonal. The set of points in space corresponding to integer combinations of the unit vectors corresponds to the *Bravais lattice*, of which there are only 32 in three dimensions. The combination of the translation symmetry embodied in the Bravais lattice with the point group symmetry of the basis gives rise to 230 space groups, which are sufficient to classify all known crystalline solids.[3]

The calculation of the properties of a huge - nearly *infinity*, number of electrons is drastically reduced by Bloch's theorem.[18] This theorem connects the properties of an infinite-crystalline solid material with those of the electrons in the unit cell. The calculation of the wave function for all the electrons in the solid is therefore mapped onto the calculation of the wave function for a finite number of electrons in the unit cell at any wave vector $\mathbf{k}$, which are in the first *Brillouin zone* (BZ). Numerically, one has to define a *Brillouin zone sampling*.

For solid state applications, the Kohn-Sham equations (eq. (2.14)) must be solved for each $\mathbf{k}$-point included in the BZ sampling. The connection emerges through the electronic density, which is now expressed as a BZ average,

$$\rho(\mathbf{r}) = \sum_{\mathbf{k} \in BZ} \omega_{\mathbf{k}} \sum_{i=1}^{N_{\mathbf{k}}} f_i^{(\mathbf{k})} \left| \varphi_i^{(\mathbf{k})}(\mathbf{r}) \right|^2, \tag{2.16}$$

where $N_{\mathbf{k}}$ is the number of electronic states occupied at each $\mathbf{k}$-point, and

$f_i^{(\mathbf{k})}$ is the occupation number of band i at wave vector $\mathbf{k}$. The weight factors $\omega_{\mathbf{k}}$ depend on the symmetry of the unit cell. If the system is insulating, then $f_i^{(\mathbf{k})} = 1$ independently of i and $\mathbf{k}$, and $N_{\mathbf{k}} = N$. If there is spin degeneracy the sum is carried up to $N/2$, and then multiplied by a degeneracy factor $f_i^{(\mathbf{k})} = 2$.

2.2 Green's Functions Approach

The *Green's functions* (GF) represent an alternative to describe the many-body system and find the propagating solutions of the Schrödinger's equation. These functions, given by $G(\mathbf{r}, \mathbf{r}'; t)$, represent the probability of having an electron at $\mathbf{r}$ at time t given that there was an electron at $\mathbf{r}'$ at time 0.[20] When Fourier-transformed into energy space, the GF for the *free* lattice is the solution to the following differential equation:

$$\left[\frac{\hbar^2}{2m} \nabla^2 + E \right] G(\mathbf{r}, \mathbf{r}', E) = \delta(\mathbf{r} - \mathbf{r}'), \tag{2.17}$$

with the boundary conditions

$$G(\mathbf{r}_S, \mathbf{r}', E) = e^{i\mathbf{k} \cdot \mathbf{T}} G(\mathbf{r}, \mathbf{r}', E), \tag{2.18}$$

$$\frac{\partial G(\mathbf{r}_S, \mathbf{r}', E)}{\partial n} = -e^{i\mathbf{k} \cdot \mathbf{T}} \frac{\partial G(\mathbf{r}_S, \mathbf{r}', E)}{\partial n}. \tag{2.19}$$

In a periodic solid, the boundary conditions correspond to a polyhedral shape, and therefore $\mathbf{r}$ and $\mathbf{r}_S$ are conjugate points on the boundary of the polyhedron. In this polyhedral, the integral problem of the wave function is computed by

$$\psi(\mathbf{r}, E) = \int_\tau G(\mathbf{r}, \mathbf{r}', E) V(\mathbf{r}') \psi(\mathbf{r}', E) d\tau, \tag{2.20}$$

where τ is the volume of the atomic polyhedral. This equation represents a sum of contributions from waves scattered from all other cells. The structural GF, inside the integral of eq. (2.20), is identical for all unit cells. This equation in principle must be recovered using variational principles using a **trial** wave function. In principle, the variational condition gives a set of linear equations whose determinant, that vanishes, is a function of the wave vector $\mathbf{k}$ and the energy thus yielding the electronic structure.

In a more general fashion, the GF is the solution of a Schrödinger-like equation

$$\left\{-\frac{\hbar^2}{2m}\nabla^2 + v_{ext}(\mathbf{r}) - E\right\} G(\mathbf{r},\mathbf{r}';E)$$

$$+ \int \Sigma(\mathbf{r},\mathbf{r}'';E)G(\mathbf{r}'',\mathbf{r}';E)d\mathbf{r}'' = -\delta(\mathbf{r}-\mathbf{r}'), \quad (2.21)$$

where $\Sigma(\mathbf{r},\mathbf{r}'';E)$ is the *self-energy* operator, which in general is a non-local, non-hermitian, energy-dependent operator.

Once the GF is known, all physical properties can be calculated. In the energy domain, the GF is the solution of the Schrödinger-like equation

This equation is recovered using variational principles, solved in the single unit cell, using a *trial* wave function that consists of a superposition of spherical harmonics and structural constants. Individual components, such as the Hartree and exchange-correlation potentials can be separated from Σ. If the exact GF $G_0(\mathbf{r},\mathbf{r}';E)$ for a related reference system is known, for instance the free-particle case given by eq. (2.17), then the required GF $G(\mathbf{r},\mathbf{r}';E)$ can be calculated through Dyson's equation:

$$G(\mathbf{r},\mathbf{r}';E) = G_0(\mathbf{r},\mathbf{r}';E)$$

$$+ \int \int G_0(\mathbf{r},\mathbf{r}_1;E)\Delta\Sigma(\mathbf{r}_1,\mathbf{r}_2;E)G(\mathbf{r}_2,\mathbf{r}';E)d\mathbf{r}_1 d\mathbf{r}_2. \quad (2.22)$$

Here, the interaction potential is given by $\Delta\Sigma(\mathbf{r}_1,\mathbf{r}_2;E) = \Sigma(\mathbf{r}_1,\mathbf{r}_2;E) - v_2(\mathbf{r}_1 1,\mathbf{r}_2)$, with $v_2(\mathbf{r}_1,\mathbf{r}_2)$ the interaction potential of the reference system.

Once we have the GF of the system, we can calculate in principle all the ground state electronic properties in the framework of the muffin-tin potential model. For instance, the spin dependent local charge distributions are calculated from the imaginary part of energy integral of the site diagonal GF:

$$\rho(\mathbf{r}) = -\frac{1}{\pi}\operatorname{Im}\int_{-\infty}^{E_F} dE\, G(\mathbf{r},\mathbf{r};E). \quad (2.23)$$

Green's functions are exactly known for non-interacting electrons and, in general, for single-particle approximations such as Kohn-Sham and Hartree-Fock. These assume the form

$$G_0(\mathbf{r},\mathbf{r}';E) = \sum_n \frac{\varphi_n(\mathbf{r})\varphi_n^*(\mathbf{r}')}{E - \varepsilon_n}, \quad (2.24)$$

where $\varphi_n(\mathbf{r})$ are the solutions of the single-particle equation and ε_n the

corresponding eigenvalues. The problem, after a suitable definition of the reference GF, reduces to compute the self-energy term which contains all the exchange and correlation effects. One way to solve this problem is, for instance, Hedin's *GW approximation* which consists of retaining the first term in an expansion of the self-energy in terms of the dynamically screened Coulomb interaction W:[21]

$$\Sigma_{GW}(\mathbf{r}, \mathbf{r}'; t) = iG(\mathbf{r}, \mathbf{r}'; t)W(\mathbf{r}, \mathbf{r}'; t) \tag{2.25}$$

The computations of the electronic properties using the GF formalism and eq. (2.23), as a generic solution of the quantum-mechanical problem, are dramatically reduced since these functions are represented in the complex space.

2.3 Multiple Scattering Methods: the KKR Method

The original work of Korringa, Kohn and Rostocker (KKR),[22,23] introduces the approximation of considering the potential as spherically symmetric inside atom-centered spheres inscribed into the atomic polyhedron, and constant in the interstitial region. Within this approximation, the atomic potential is represented by a superposition of spherically symmetric *muffin-tin* (MT) potentials, $V = \sum V_i$, where V_i is centered at any atomic position. Within this MT approximation, the Schrödinger's equation is solved in a periodic lattice using a variation-iteration method and yields a set of simplified equations to determine the structural constants and therefore the electronic structure.

Inside the spheres, in an angular momentum basis, the solutions for the orbitals are expanded into one-center partial waves

$$\varphi(\mathbf{r}, E) = \sum_{l=0}^{l_{max}} \sum_{m=-l}^{l} C_{lm} \overline{\chi}_l(r, E) Y_{lm}(\hat{\mathbf{r}}), \tag{2.26}$$

where the functions $\overline{\chi}_l(r, E)$ are regular solutions of the radial Schrödinger equation for energy E in the presence of the spherical MT potential. There is a set of coefficients C_{lm}^I for each atom I in the unit cell. The GF is expanded in spherical harmonics around $\mathbf{r}$ and $\mathbf{r}'$. This is done using the spherical Bessel and Neumann (and Hankel) functions. This leads to a non-trivial set of linear equations, which have a solution in the KKR secular equation.

In turn, The GF is expanded in spherical harmonics and, outside the MT potential range, the radial Schrödinger equation is that of a free particle. In this method, it is supposed that the crystal is composed of an assembly of non-overlapping MT potentials centered on each lattice site. The crystal GF $G(\mathbf{r}, \mathbf{r}'; E)$ can be calculated from the free space solution $g(\mathbf{r}, \mathbf{r}'; E)$ using a Dyson equation similar to that given by eq. (2.22).

Expanding this function in spherical harmonics, this equation yields the contribution due to the multiple scattering giving rise to the band structure.

In the angular-moment $(L = (l, m))$ representation, the structural GF read

$$G_{LL'}(\mathbf{k}) = \sum_{L''} g_{LL''}(\mathbf{k}) \left[1 - tg(\mathbf{k})\right]^{-1}_{L''L'}, \qquad (2.27)$$

where t is, by definition, the atomic t-matrix which describes the scattering of the MT atoms. Standard KKR band structure calculation is performed by finding the zero of the determinant of the KKR matrix for each $\mathbf{k}$ vector

$$\det \left|\delta_{LL'} - t_L(E) g_{LL'}(\mathbf{k}; E)\right| = 0. \qquad (2.28)$$

The zeros of the KKR matrix give the poles of the GF in a one-to-one correspondence. This determinant is rather simplified algebraically. However, the actual formula is very complicated since it involves Clebsch-Gordan coefficients and spherical Bessel functions. To evaluate the lattice sums, the Ewald method is used.

In the KKR method we sum over reciprocal lattice vectors, by a Fourier transformation. This method requires a high-performance computer. The advantage of this method is that structural and atomic properties can be separately computed and combined quickly.

There are plenty of details about this formalism, specially those coming from the theory. A vast literature about this topic can be found,[24] since it represents the basis of the multiple-scattering theory that can be applied to a large number of physical phenomena, e.g., transport. The main experience of the group, AG Heiliger, lies in this DFT-based GF that nowadays is implemented for a large variety of situations. For instance, the bare band structure computations that require the computation of a reference single-electronic GF. The actual GF of the system requires the inclusion of exchange and correlation effects extracted from the functionals introduced in section 2.1. The muffin-tin potential is also generalized to a full-potential approximation

that accounts for the angular-momentum expansion in the interstitial regions. Moreover, full-relativistic effects have also been implemented in this formalism that accounts for the spin-orbit effects on the bands, and other relevant terms that shift the single-electronic energies.[25] There are several further functionalities and possibilities inside this formalism that have been worked out during the last years, even decades, that nowadays provide a very powerful tool to determine the electronic and transport properties of materials and alloys.

2.4 Coherent Potential Approximation

There are different alternatives in DFT to describe the physical properties of systems with chemical disorder such as alloys. For instance, site atomic substitutions between different atoms, or impurities, create a local distortion of the crystal lattice and a breakdown of its translational symmetry. The electronic properties of such an impurity are suitably accounted for when the impurity is considered to be embedded in a larger supercell, and the computations comprehend all possible ensemble configurations. Though this approximation is consistent with any electronic band structure theory, the computational cost is very high with unavoidable effects on the band structures, such as zone folding.[26]

The *virtual crystal approximation*, on the other hand, describes the alloys using an effective medium representing a simple average of the alloy components, but disorder effects are neglected.[27,28] Disorder effects are accounted for when a statistical average over all possible on-site occupancies of the alloy are considered and thereby all possible configurations. This indicates that the theory must be sensitive to average quantities rather than detailed microscopic configurations of the alloy.

A soluble and thermodynamically stable substitutional alloy between the atoms A and B of the form $A_{1-x}B_x$, with concentrations c_A and c_B, respectively, is considered here. In this alloy, an underlying crystal symmetry exists, with short-range order distortions, defined by sharp Bragg peaks in the diffraction pattern. The *coherent potential approximation* (CPA) consists of a formal replacement of the t-matrix at each alloy site by an effective $\bar{t}$ that represents the perturbing potential of the atom A or B away from a reference *unknown* potential. This unknown potential must de defined to find the exact alloy GF using the multiple-scattering theory.

The CPA condition states, that to find the reference potential of the alloy system, and therefore the alloy GF, a self-consistent system of equations must be solved. This system demands that on the average there

is no further scattering, i.e., $c_A \bar{t}_A + c_B \bar{t}_B = 0$, and therefore it is possible to approximate the ensemble average of the alloy GF to the actual alloy GF with the self-consistent potential. With this approximation, the resulting GF will simulate the electronic properties of the actual alloy.[29]

This method has been implemented in the KKR,[30] within the single-site approximation (SSA) that decouples the averaged multiple-scattering expansion.[31] Therefore, the SSA implies that the occupation probabilities at each site are independent from each other. One consequence of the SSA is that this approximation does not account for short-order effects like clustering.

In a general scheme, the modified propagator consist of a formal replacement of $(E - k^2)^{-1} \rightarrow [E - k^2 - v_C(k, E)]^{-1}$, where $v_C(k, E)$, the coherent potential, which is a complex quantity describing the average effects of the medium. It is a complex, energy-dependent quantity, and has been introduced as a model as an attempt to create an scheme whereby the charge density and the *position* of the energy bands could be determined. Consequently, $v_C(k, E)$ is not a real physical potential.

Since now the electronic band structure is complex, and the electronic wave number $\mathbf{k}$ is not uniquely defined, the physical quantities must be obtained from a Bloch spectral-density (BSF) function $A(E, \mathbf{p})$, given by

$$A(E, \mathbf{p}) = -\frac{1}{\pi N \tau} \operatorname{Im} \int \int e^{e\mathbf{p} \cdot (\mathbf{r} - \mathbf{r}')} G(E, \mathbf{r}, \mathbf{r}') dv dv'. \tag{2.29}$$

Here, N represents the number of unit cells in the crystal. The BSF allows to map a band structure since it is, by definition, a $(\mathbf{k}, E)$-resolved charge density.

2.5 Phonons

In DFT, the ground state electronic density and wave functions of a crystal are found by solving self-consistently a set of one-electron equations, as presented in section 2.1. The calculation of reliable phonon properties of materials is well within the reign of DFT.[32] It is now possible to obtain accurate phonon dispersion on a grid of wave vectors covering the entire BZ, which compare directly with neutron-diffraction data, and from which several physical properties of the system, such as heat capacities and thermal expansion coefficients, can be calculated. The key assumption is the validity of the Born-Oppenheimer approximation, which views a lattice vibration as a static perturbation on the electrons, and the knowledge of the linear response of the system to a small displacement. It is well known that the harmonic force constants of

crystals are determined by their static linear electronic response. Within the Born-Oppenheimer approximation, the lattice distortion associated with a phonon can be seen as a static perturbation acting on the electrons.

Once the unperturbed ground state is determined, phonon frequencies can be obtained from the interatomic force constants, i.e., the second derivatives at equilibrium of the total crystal energy versus displacements of the ions,

$$C_{\alpha i,\beta j}(\mathbf{R} - \mathbf{R}') = \left.\frac{\partial^2 E}{\partial u_{\alpha i}(\mathbf{R})\partial u_{\beta j}(\mathbf{R}')}\right|_{equil} = C^{ion}_{\alpha i,\beta j}(\mathbf{R}-\mathbf{R}')+C^{elec}_{\alpha i,\beta j}(\mathbf{R}-\mathbf{R}'),$$

(2.30)

where $\mathbf{R}(\mathbf{R}')$ corresponds to a Bravais lattice vector, $i(j)$ indicates the ith (jth) atom of the unit cell, and $\alpha(\beta)$ represents the Cartesian component. $C^{ion}_{\alpha i,\beta j}$ are the second derivatives of Ewald sums corresponding to the ion-ion repulsion potential, while the electronic contributions $C^{elec}_{\alpha i,\beta j}$ are the second derivatives of the electron-electron and electron-ion terms in the ground state energy.[33] From the Hellmann-Feynman theorem,[34,35] one obtains the phonon frequencies at any $\mathbf{q}$ on the solutions of the eigenvalue problem

$$\omega^2(\mathbf{q})u_{\alpha i}(\mathbf{q}) = \sum_{\beta j} u_{\beta j}(\mathbf{q})\widetilde{D}_{\alpha i,\beta j}(\mathbf{q}).$$

(2.31)

The Hellmann-Feynman theorem states that the *force* associated with the variation of the external parameters, such as ion displacements, is given by the ground state expectation value of the derivative of the external potential acting on the electrons v_{ext}.

Linear response theory allows us to calculate the response to any periodic perturbation; i.e., it allows direct access to the dynamical matrix related to the interatomic force constant via a Fourier transform,

$$\widetilde{D}_{\alpha i,\beta j}(\mathbf{q}) = \frac{1}{\sqrt{M_i M_j}} \sum_{\mathbf{R}} C_{\alpha i,\beta j}(\mathbf{R})e^{-i\mathbf{q}\cdot\mathbf{R}}$$

(2.32)

with $M_i(M_j)$ the mass of the atom $i(j)$. Phonon frequencies at any $\mathbf{q}$ are the solutions of the eigenvalue problem eq. (2.31). In practice, one calculates the dynamical matrix in the BZ, and obtains the corresponding interatomic force constants by inverse Fourier transform. Finally, the dynamical matrix (and phonon frequencies) at any $\mathbf{q}$ point can be obtained by Fourier interpolation of the real-space interatomic force constants.

There exists also the density-functional perturbation theory (DFPT),[36] in which the linear density response of the system to an external perturbation is calculated self-consistently via the solution of a set of equations, which involve as known terms only quantities related to the unperturbed crystal.

To compute the thermodynamic properties of the system, when there is no external pressure, the equilibrium structure at any temperature T can be found by minimizing the Helmholtz free energy $F(\{a_i\}, T) = U - TS$ with respect to all its geometrical degrees of freedom $\{a_i\}$.[33]

2.6 Total Energy Calculations

The equilibrium lattice structure at $T = 0$ is determined by minimizing the crystal total energy $\varepsilon(V)$ as a function of the structural volume. For this purpose, the values of the total energy calculated for different lattice constants have been fitted to the Murnaghan-Birch equation of state,[37,38]

$$\varepsilon(V) = \frac{V_0 B_0}{B_0'} \left[\frac{1}{B_0' - 1} \left(\frac{V_0}{V} \right)^{B_0' - 1} + \frac{V}{V_0} \right] + \text{const}, \qquad (2.33)$$

where B_0' is the derivative of the bulk modulus with respect to the pressure.

A great variety of physical quantities of solids depends on their lattice-dynamical behavior, to mention a few of them, infrared, Raman, and neutron-diffraction spectra. As well, phenomena related to electron-phonon interaction such as the resistivity of metals, superconductivity, and the temperature dependence of optical spectra are just a few of them.[39]

3 Results and Discussion

In this chapter I present the main results obtained using the theoretical machinery described in the last section, applied to the specific problems proposed by the RTG2204 group. The parts that I present below have been either already published or are yet in preparation for publication. In a short way I will present them without exhaustive technical details, such as computational tools, convergence tests, optimization of computational times, and specially all kind of errors that can be found during the progress of the research. I have compacted the information in a practical way not necessarily using an strict chronological order of discovery but rather a logical order.

The first application presented here corresponds to a collaborative research with Prof. Dr. Eckhard Müller and his research team in the field of thermoelectric properties of magnesium silicide alloys. This field remains as an active field after several decades since there are still many fundamental scientific questions about the functionality and possible applications of these alloys. The approach that I adopt here allows to obtain new information about the electronic and structural components. These results account very well for the scarce experimental trends and predict those properties that are still out of the experimental scope.

The second application made during my doctoral training relates to Raman spectroscopy and finds a direct application to the case of graphene samples. This project is driven by a direct collaboration with Prof. Dr. Peter J. Klar and his research group at the University of Giessen, that thereby enabled me to have access to the experimental data. The main goal was to demonstrate that the Raman selection rules can be obtained from the equilibrium electronic and phonon properties of graphene, and elemental conservation rules. Under this assumption, the micro-crystalline effects on the Raman signals are accounted for using a line-shape modeling that involves the relaxation of the conservation rules through a phonon-confinement model. This model is system independent and allowed me to model the micro-crystalline effects on further systems, not presented here, like CeO_2 and diamond. As is expected in research, the scope of this work potentially embraces other experiments currently performed in the RTG2204 group.

3.1 Electronic properties of Thermoelectric Mg$_2$X

In this section I present the main results of my research about electronic and structural properties of the green-thermoelectric semiconductors Mg$_2$X, for X = Si, Ge, Sn, and their intermediate quasi-binary alloys. The main motivation of this project is the need for sustainable and environmentally friendly materials that substitute conventional raw elements in industry.

From the practical point of view, silicon-based materials are desirable for technological applications since silicon is one of the most abundant elements in the earth crust. However, its low thermoelectric efficiency still precludes this material for a large-scale production of thermoelectric devices. It has been found that the iso-electronic Ge and Sn elements, both less abundant and more expensive than Si, are the best substitutions for Si in the quasi-binary Mg$_2$Si$_{1-x}$Y$_x$ compounds, with Y = Ge, Sn.

Another limitation found in these materials is the structural-miscibility gap found in Mg$_2$Si$_{1-x}$Sn$_x$ and Mg$_2$Ge$_{1-x}$Sn$_x$, not present in Mg$_2$Si$_{1-x}$Ge$_x$, that consist of a thermodynamic unstable state that tends to separate the alloy into individual Mg$_2$X-compounds.

For this study, I performed DFT-based calculations that account for the structural stability and the electronic properties. Within the framework of the Green's function based Korringa-Kohn- and Rostoker (KKR) method in full relativistic description, I compute the electronic properties of the Mg$_2$X semiconducting compounds. I describe the influence of chemical disorder on the bands using the coherent potential approximation (CPA) implemented in the KKR code. Within this formalism I extract the electronic structure parameters relevant for transport, such as total formation energies, optimal unit cell volumes at intermediate compositions, forbidden band gap energies, and effective masses of the conduction and valence bands in the vicinity of the Fermi level.

3.1.1 Introduction

In the last years there has been an increasing interest in the transport properties of Mg$_2$X$_{1-x}$Y$_x$ green-thermoelectric materials, for X, Y = Si, Ge, Sn. They are indirect band gap semiconductors, crystallize in the anti-fluorite structure[40], and have attracted much attention as candidates for thermo-electric applications in the mid temperature range 500 to 800 K.[41,42] Among the Mg$_2$X raw materials, Mg is one of the most abundant metals

in the earth crust, but hazardous in its pure state. group IV materials are non-toxic and environmentally sustainable,[43,44] but pure Ge can exceed the price of Si by a factor of ~ 800, or in the case of Sn by a factor of ~ 70. Further, its abundance is substantially lower, even though it is one of the best substitutes of Si.[45,46]

Early experiments, using the Hall effect,[47–49] electrical resistivity,[50–53], and the electro-reflectance techniques,[54–56] evidence the *n*-type nature of the nearly pure Mg$_2$Si,[48,57–59] Mg$_2$Ge,[49,57] and Mg$_2$Sn compounds.[51,60] These materials support *p*-type of transport under doping by a metallic element, like Ag or Cu, as required for the manufacturing of thermo-electric devices.[61,62] However, *p*-type samples have not shown excellent performance.[63]

Contemporaneously, different semi-empirical computational tech-niques were used to interpret and corroborate the measurements on Mg$_2$X with a good agreement.[64–70] More recently, modern density func-tional theory (DFT) techniques have also been employed to compare the accuracy of the exchange-correlation potential and its effects on electronic properties and transport.[71–75]

It was furthermore well known that relativistic effects had an important impact on the electronic bands,[70] such as degeneracy lifting of valence bands, and shifts in the charge's velocities and effective masses.[76] A brief summary of some physical quantities from early studies on crystalline Mg$_2$X is gathered in table 3.1.

Even though the studies have been mainly focused on nearly pure Mg$_2$X samples, early experiments on inter-metallic compounds have manifested their enhanced thermoelectric properties[47] that have been crucial for technological applications.[77–79] A detailed study demonstrated the complete solubility of the Mg$_2$Si$_{1-x}$Ge$_x$ system for all intermediate compositions, and confirmed their *n*-type nature and similarity of their band structure.[42,80–83] The band gap in these alloys remains nearly constant, at a value of 0.75 ± 0.05 eV, and the structural parameters obey the empirical Vegard's law.[84]

In the Mg$_2$Si$_{1-x}$Sn$_x$ and Mg$_2$Ge$_{1-x}$Sn$_x$ systems, no complete solubility has been found.[40] Solubility is still under debate, since it has been demonstrated that solid solutions of any composition can be produced under mechanical alloying.[80,86–88] In these systems, the degeneracy and inversion of conduction bands lead to high-performance thermoelectric properties[89] at a composition close to $x = 0.65$,[40,90–92] not observed in Mg$_2$Si$_{1-x}$Ge$_x$,[77,93] as confirmed theoretically.[94] It has also been seen in that system, that the band-gap decreases non-linearly with larger substitution of a heavier Y element.[79] In such a way, the effective mass

3 Results and Discussion

TABLE 3.1: Experimental and theoretical data of crystalline samples of Mg_2X from literature, corresponding to the lattice constant (a), indirect (E_I), direct (E_D), and low-lying conduction (E_X) band gaps, spin-orbit (E_{SO}) energy splitting, and hole/electron effective masses $m_{p,n}$. Theoretical n-type effective masses ($m_\parallel$ and $m_\perp$) correspond to electronic bands at the bottom of the conduction bands. Empty spaces correspond to unavailable data. Table taken from reference [E1].

| | Mg_2Si | | Mg_2Ge | | Mg_2Sn | |
	Exp	Theo	Exp	Theo	Exp	Theo
a (Å)	6.340[47]	6.160[66]	6.385[47]	6.310[71]	6.765[47]	6.730[71]
E_I (eV)	0.780[48]	0.530[67]	0.600[49,50]	0.920[67]	0.330[51]	0.640[67]
E_D (eV)	2.170[52]	2.060[67]	1.700[50,52]	1.630[72]	1.200[52]	1.060[67]
E_{SO} (eV)	0.030[52]	0.036[85]	0.200[52,54]	0.208[85]	0.800[55]	0.525[85]
E_X (meV)	0.400[44]	0.670[65]	0.580[44]	0.780[65]	0.160[44]	0.276[73]
m_n (m_0)	0.46 [48,58]	–	0.18 [49]	–	1.17 [51]	–
$m_\parallel$ (m_0)	–	0.69 [65]	–	0.63 [65]	–	–
$m_\perp$ (m_0)	–	0.25 [65]	–	0.25 [65]	–	–
m_p (m_0)	0.87 [48,58]	–	0.31 [49]	–	1.28 [51]	–

remains nearly constant,[95] and the lattice constant varies linearly with composition.[73,96]

In order to improve the thermoelectric properties of these alloys and to suppress bipolar contribution to transport, a great theoretical and experimental research effort has been devoted[97–99] to study the most efficient dopants and the intrinsic/extrinsic defects in n- and p-type regimes[100–108] near the band crossing.[109–113] Different *ab initio* techniques have been employed to study structural stability and to extract relevant transport parameters in these compounds. Supercell methods have shown zone-folding effects on bands, and have confirmed the crossing of conduction bands in $Mg_2Si_{1-x}Sn_x$[114,115] and $Mg_2Ge_{1-x}Sn_x$.[116] Chemical disorder has also been addressed using DFT- special quasi-random structures,[114,117,118] as well as the coherent potential approximation in the framework of the Green's functions formalism.[119]

Since some intermediate transport parameters are still unknown, or the quantitative trends are not clear enough, I investigate the possibility of modeling the electronic properties of $Mg_2X_{1-x}Y_x$ alloy systems using an effective single parabolic band (SPB) approximation.[62,120] Even though experiments have evidenced clustering, or pure Mg_2X-rich regions, at some compositions,[121] I rely on the homogeneity of the alloys and extend the rigid-band structure approach to map the bands of the intermediate alloy systems using a Bloch spectral density function (BSF) defined within the coherent potential approximation (CPA),[29,30]

implemented in the Korringa-Kohn-Rostoker (KKR) formalism in the full-relativistic case.[25,122] I compare my results with those already obtained by experiments and calculations, and give an interpretation based on the limitations of the formalism. The agreement between the existing data and the present calculations is very good and indicate that the calculated quantities can be used as a basis for interpreting further experimental results.

3.1.2 Theoretical Details

Mg$_2$X crystalline materials, for X = Si, Ge, Sn elements in group IV A of the periodic table, are narrow indirect band-gap semiconductors and all crystallize with anti-fluorite (CaF$_2$) structure. The constituent X-atoms occupy FCC sites at $(0, 0, 0)a$, while remaining Mg atoms are located at $(\frac{1}{4}, \frac{1}{4}, \frac{1}{4})a$ and $(\frac{3}{4}, \frac{3}{4}, \frac{3}{4})a$, where a is the cubic lattice constant; experimental and theoretical physical properties of these materials are collected in table 3.1. The resulting structure has space group symmetry O_h^5 ($Fm\overline{3}m$) (group number 225), closely related to diamond structure[66]. For a systematic analysis of substitutional alloying between the crystalline materials, I use the CPA[29,30] implementation in the KKR framework[25,122] that is in accord with supercell or special quasi-random structure methods[114,116] and provides a very efficient and computational time saving method for the description of the alloys, but does not consider local effects like clustering. The local density approximation (LDA) is used for treating the exchange-correlation energy functional.[123] I use a full-relativistic description, and a k-space mesh of $48 \times 48 \times 48$ for BZ integration. It is well known that the LDA yields quite reliable ground-state properties, but underestimates the band gap and lattice constants for most usual semiconductors, compared to the general gradient approximation (GGA) or *GW* methods.[72,73,93]

3.1.3 Band Structure Details

Since the Brillouin zones of Mg$_2$X are identical,[40] the band structures are similar and can be described around Γ and X (face [001]) points, close to the Fermi level, as illustrated in fig. 3.1; detailed electronic band structures have been already presented and studied elsewhere, and the Fermi level is set at the top of the valence bands.[76,85] My computed quantities are summarized in table 3.2, for crystalline materials and intermediate solid solutions.

Qualitatively speaking, at the Γ point one finds the bottom of the
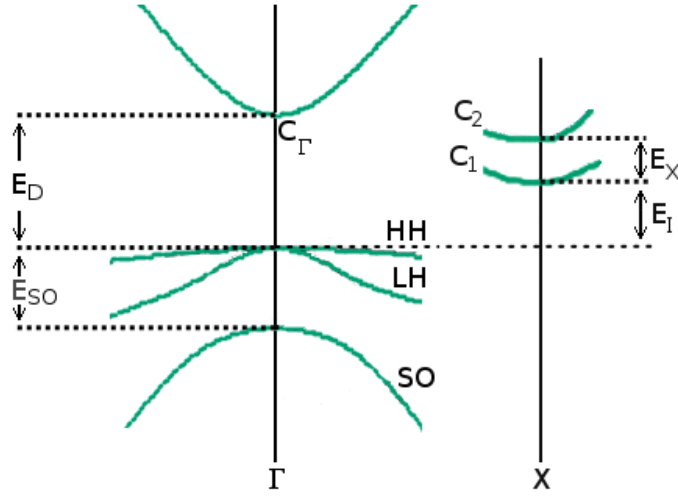
FIGURE 3.1: Schematic band structure of crystalline Mg_2X in the vicinity of the center of the BZ and the X-point. Figure taken from reference [E1].

conduction band C_Γ, with symmetry Γ_1,[65–67] and the top of the valence bands at Γ_{15}, that define the direct band-gap (E_D) as the transition $\Gamma_{15} \to \Gamma_1$. The top of the valence bands consists of two degenerate bands at the Γ-point, labeled as heavy-hole (HH) and light-hole (LH) bands, and a lower split-off (SO) band separated by an energy gap (E_{SO}) ranging from 0.03 to 0.8 eV for different compounds (see table 3.2).

The valence bands of Mg_2X are mainly composed by p-X states, but also small contributions of s- and p-Mg states. s-X states contribute weakly to HH, LH, and SO bands, but strongly form the density of states (DOS) at deep energies (~ -8 eV).[91,114,124] The X point is composed by two low-lying conduction bands labeled as C_1 and C_2, with symmetries X_1 and X_3 respectively, separated by a distance E_X, that define the indirect band-gap (E_I) as the transition $\Gamma_{15} \to X_{1,3}$. The lowest conduction band in Mg_2Si (Mg_2Ge) is a hybridized s-Mg-p-Si (s-Mg-p-Ge), followed by a mostly s-Mg band at an energy E_X above. This unoccupied, mainly 3s-Mg band, is pushed down in Mg_2Sn and is lower in energy than the hybridized s-Mg-p-Sn; therefore these bands, C_1 and C_2, are inverted in the compounds Mg_2Si (or Mg_2Ge) and Mg_2Sn. DOS calculations show that the effective mass of p-type carriers must be larger than that of n-type, since the slope of the total charge density below the Fermi level exceeds the slope above the Fermi level.[91]

3.1.4 Total Energy Calculations

I obtain optimal structural properties of pure and intermediate alloys by minimizing the total energy of the system with respect to the lattice constant of the unit cell. Minimization of the total energy with respect to small variations of the unit cell volume allows one to find the optimal structural properties. Total energy calculations are also powerful to obtain structural properties such as the bulk modulus and its derivative, using a Murnaghan-Birch equation of state,[119] as it was introduced in section 2.6. However, these quantities are better described using multipole moment and full-potential corrections, and I limit my calculations here to the atomic sphere approximation (ASA) that seems to show good agreement with available experimental data. Here I consider the on-site substitution between the *X*-elements, since it has been demonstrated that this kind of defect (X$_Y$) are thermodynamically more likely to occur than the Mg-Y substitutions (Mg$_Y$).[104,125,126]

Using the KKR-DFT total energy E, I computed the formation energy of the Mg$_2$X elements, obtained in the reaction $2\,\mathrm{Mg} + \mathrm{X} \rightarrow \mathrm{Mg_2X}$, using $E_{form} = E(\mathrm{Mg_2X}) - 2E(\mathrm{Mg}) - E(\mathrm{X})$. However, in order to study the thermodynamic stability, the atomic chemical potentials (μ) should be considered to vary under specific constraints of the material in the bulk and dilute phases.[127,128] Therefore, I generalize the formation energy formula of the Mg$_2$X$_{1-x}$Y$_x$ alloys, obtained in the reaction

$$2\,\mathrm{Mg} + (1\text{-}x)\mathrm{X} + x\mathrm{Y} \rightarrow \mathrm{Mg_2X_{1-x}Y_x}, \qquad (3.1)$$

and I use

$$E_{Form} = E(\mathrm{Mg_2X}) - 2\mu(\mathrm{Mg}) - (1-x)\mu(\mathrm{X}) - x\mu(\mathrm{Y}). \qquad (3.2)$$

Since the substitution is between X$_Y$-elements, I have to consider the bulk phase of Mg, and therefore, together with eq. (3.2), the restrictions to the chemical potentials in the Mg-rich region are given by

$$\mu(\mathrm{Mg}) = E(\mathrm{Mg})$$
$$\mu(\mathrm{X}) = E(\mathrm{Mg_2X}) - 2E(\mathrm{Mg}) \qquad (3.3)$$
$$\mu(\mathrm{Y}) = E(\mathrm{Mg_2Y}) - 2E(\mathrm{Mg})$$

so that the formation energy of the binary crystals, $x = 0$ and $x = 1$, vanishes. Note that the formation energy, given by eq. (3.2), under the

restrictions given by the thermodynamical chemical potential given by eq. (3.3), is equivalent to

$$E_{Form} = E\left(Mg_2X_{1-x}Y_x\right) - (1-x)E(Mg_2X) - xE(Mg_2Y), \quad (3.4)$$

as I computed for all compounds, as presented in fig. 3.2. In contrast to the reported trend, $\left|E_{form}^{Mg_2Si}\right| < \left|E_{form}^{Mg_2Sn}\right| < \left|E_{form}^{Mg_2Ge}\right|$,[126] my calculations predict that $\left|E_{form}^{Mg_2Sn}\right| < \left|E_{form}^{Mg_2Si}\right| < \left|E_{form}^{Mg_2Ge}\right|$. Both results agree very well with the experiments in the sense that the formation energies of Mg_2Si and Mg_2Sn are very similar.[80]
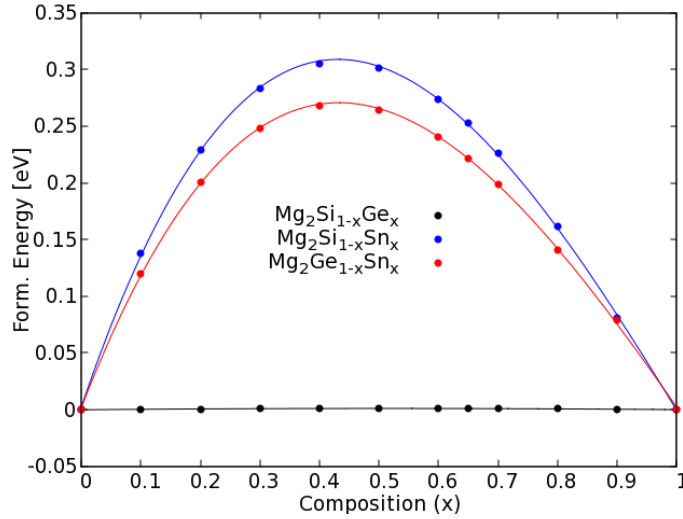
FIGURE 3.2: Formation energy of the intermediate $Mg_2X_{1-x}Y_x$ alloy compositions. The solid lines represent the cubic polynomial fit. Figure taken from [E2]

As presented in fig. 3.2, I measure the relative formation energy, from total energy calculations, and the result shows the complete solubility of the $Mg_2Si_{1-x}Ge_x$ compounds. In contrast, intermediate compounds of the families $Mg_2X_{1-x}Sn_x$ show larger formation energies thus indicating that, energetically speaking, it is more likely to find those compounds lying at lower formation energies, close to 0, in order to avoid a decomposition into pure Mg_2X-materials.[40,80,129–131] These results look qualitatively similar to the present formation energy calculations, but, as similarly

defined in literature,[104] I allow the chemical potentials to vary in the Mg$_2$X-rich phases, and adapt this definition for the general Mg$_2$X$_{1-x}$Y$_x$ case.

Of course, a stability diagram analysis must include temperature effects in the free energy. Therefore, one has to evaluate relevant contributions coming from the phonon entropy. This is in principle possible to predict the solid-state phase of these intermediate compounds. However, this survey would require a complete and detailed study of the free energy landscapes using the tools from thermodynamics and kinetics.[132]

Total energy calculations have also been presented using supercell DFT calculations, in the general gradient approximation (GGA), showing a linear increase with composition for Mg$_2$Si$_{1-x}$Ge$_x$, indicating the complete solubility of these intermediate alloys.[42,80] I fitted all formation energy calculations of fig. 3.2 using a third-order polynomial similar to eq. (3.5) and the results show a maximum close to $x \sim 0.43$ for Mg$_2$X$_{1-x}$Sn$_x$, for X = Si, Ge. This maximum is also predicted to be located at $x \sim 0.3$ for Mg$_2$Si$_{1-x}$Sn$_x$,[104] and, in general terms, these results also show a very good agreement with formation energy obtained using DFT-GGA calculations.[133] Even though, using the KKR-CPA formalism, I am allowed to compute total free energy of the system and account for important state parameters, such as the optimal unit cell volumes, some other quantities are still away from the scope of this study. This is the case, for instance, of the bulk modulus or its derivative, that require detailed contributions of the lattice energy that, so far, have been ignored. Therefore, I limit myself here to the predictions that show very good agreement and that explain with good accuracy the electronic component of the systems.

3.1.5 Disorder Effects on Bands and Lattice Constant Minimization

With the total energy calculations presented in the last section, I obtained the minimized unit cell volume and from it the optimized lattice constant of a set of intermediate compounds in the Mg$_2$X$_{1-x}$Y$_x$ family. As presented in table 3.2, for the pure cases, I obtain a lattice parameter 2.1% below the experimental value for the Mg$_2$Si case, while 1.37% and 0.14% for the Mg$_2$Ge and Mg$_2$Sn cases, respectively. I found underestimations of lattice constants and energy gaps in the usual range of LDA, and dependent on the composition x, due to strong hybridization of p-X and s- and p-Mg states.[71,75,80,99,134] These underestimations are partly corrected or even overestimated by the GGA[73,75,93,107,114,115,124,135,136], and the

values of band gaps are even more accurate in the GW computational method.[72] In spite of this underestimation problem, I retain the LDA since the shape of the bands is not substantially changed at the Γ- or X-points.[76]

TABLE 3.2: Computed physical quantities of pure materials and quasi-binary alloy systems of Mg$_2$X$_{1-x}$Y$_x$: the lattice constant (a), direct energy gap (E_D), the spin-orbit splitting of valence bands (E_{SO}), and the energy gap between the low-lying conduction bands (E_X). For intermediate compositions, I fitted the data using the cubic polynomial $p(x)$, given by equation (eq. (3.5)), with non-vanishing fitting parameters α and β. Computations and fitting coefficients of band- and direction-dependent effective masses are presented as well. The cases in which $\alpha = 0.0$ and $\beta = 0.0$ are linearly-fitted. This table has been taken and modified from [E1].

	Mg$_2$Si	Mg$_2$Ge	Mg$_2$Sn	Mg$_2$Si$_{1-x}$Ge$_x$		Mg$_2$Si$_{1-x}$Sn$_x$		Mg$_2$Ge$_{1-x}$Sn$_x$	
				α	β	α	β	α	β
a (Å)	6.206	6.297	6.755	0.042	0.054	0.529	0.222	0.494	0.228
E_D (eV)	1.999	0.875	0.904	0.0	0.0	−0.023	−0.017	−1.630	−1.810
E_{SO} (meV)	0.035	0.203	0.509	0.0	0.0	0.0	0.0	0.0	0.0
E_X (eV)	0.588	0.674	0.165	0.019	0.020	0.0	0.0	0.0	0.0
Effective mass along ΓL (m_0)									
Conduction (*C*)	0.349	0.174	0.202	0.0	0.0	0.0	0.0	0.0	0.0
Light Hole (*LH*)	−0.459	−0.202	−0.193	0.305	−0.006	0.482	0.045	0.232	0.154
Split-Off (*SO*)	−0.367	−0.349	−0.487	−0.332	−0.087	−0.357	0.029	0.303	0.082
Heavy-Hole (*HH*)	−2.250	−2.287	−1.690	−0.134	−0.331	−0.411	−0.105	−0.250	−0.082
Effective mass along ΓX (m_0)									
Conduction (*C*)	0.331	0.156	0.193	0.0	0.0	0.0	0.0	0.0	0.0
Light Hole (*LH*)	−0.459	−0.220	−0.230	0.035	0.024	0.259	0.149	0.301	0.240
Split-Off (*SO*)	−0.533	−0.386	−0.505	−0.096	−0.035	0.506	−0.028	−0.068	−0.322
Heavy-Hole (*HH*)	−0.762	−0.781	−0.588	−0.060	−0.019	−0.196	−0.065	−0.131	−0.048

While direct band gaps are underestimated as 7.88% in Mg_2Si, 48.5% in Mg_2Ge, and 24.7% in Mg_2Sn, I observe that the direct band gap shrinks by nearly 18.6% and 30% for X = Si, Ge, respectively, while their indirect band gap is slightly enhanced by 8.15% and 8.90%. The differences in the bands of Mg_2Sn are not so prominent since the optimized and empirical lattice constants are similar, and the corresponding electronic band structures are similar as well.

Within the CPA approximation, as it was introduced earlier in section 2.4, it is possible to account for alloy effects on the bands thus implying that the wave vector k is not a good quantum number any more.[137] The broadening of bands is physical, and if it is small enough, one can fit the electronic parameters to an effective value, as I do in the following. If this were not possible, then a description with a SPB model would no longer be valid and thus a mapping impossible. Since in all compounds the shape and location of the LH and HH valence bands are similar, I expect alloying effects to be negligible compared to the *parabolic energy window*. I regard the parabolic shape to hold up to $k \approx 0.03(2\pi/a)$, within an energy window of ~ 100 meV, under the criteria that non-parabolic effects are rather small.[138] The parabolic shape of the bands and their effects on transport has already been tested in Mg_2X, using models of single and multiple valleys and parabolic bands for transport.[85,89,113,114,120,139–143] Non-parabolic effects have also been studied and reported to be relevant in the low-lying conduction bands.[89,138]

The broadening of the HH and LH bands is nearly homogeneous and on the order of 1% in the range of parabolicity. In contrast, SO energy bands move down with composition x, and at intermediate values they are strongly k-dependent with a smearing up to nearly 100% far from Lorentzian, as I present in fig. 3.3. This relative measurements of the alloying effects allows to determine whether it is reasonable or not, to map a band structure to a SPB model. In general, I have found well-defined bands in the $Mg_2Si_{1-x}Ge_x$ system, with smearing close or below 1%, since the change of the lattice constant with composition is not as large as in the remaining $Mg_2X_{1-x}Sn_x$ (X = Si, Ge) cases; in these cases, alloying effects are stronger specially in the SO and conduction bands at Γ hence the mapping of the bands is a numerical challenge. For small broadening in the bands, I perform a Lorentzian fit over all the intermediate k-points along different paths to map a band structure. The corresponding effective mass values will be presented below.

For the computed lattice constants shown in fig. 3.4, I find deviations from the linear Vegard's law $a(x) = a_1(1 - x) + a_2x$.[84] The data fits a
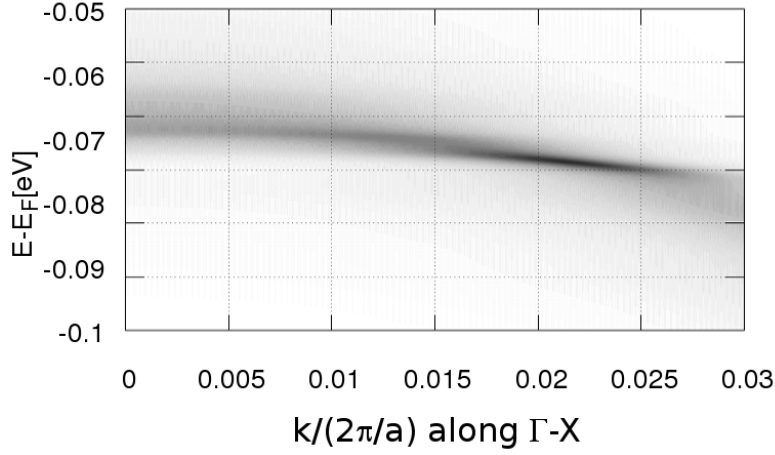
FIGURE 3.3: Example of the broadening induced by alloying effects on the *SO* band of Mg$_2$Ge$_{0.6}$Sn$_{0.4}$ (dark gray corresponds to high BSF in a.u.). Figure taken from reference [E1].
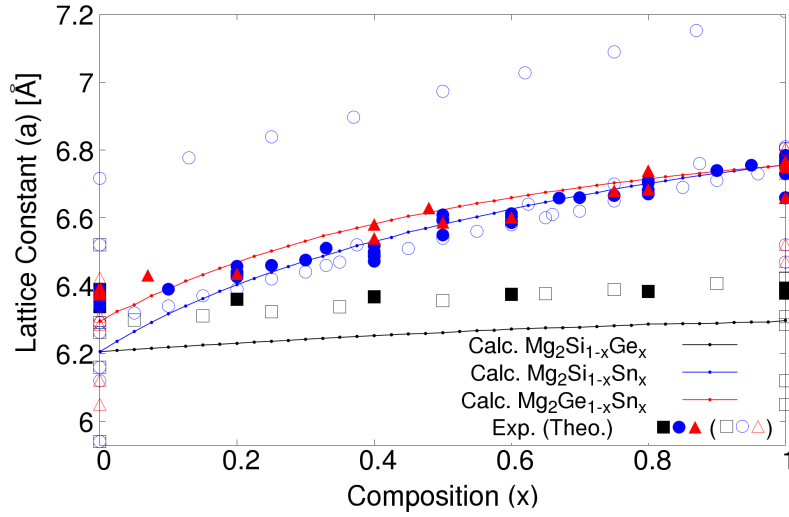

FIGURE 3.4: Computed lattice constant of the Mg$_2$X$_{1-x}$Y$_x$ systems. Experimental values of the Mg$_2$Si$_{1-x}$Ge$_x$ case are represented by solid black squares,[41–43,47,48,87,92,144] while theoretical values are represented by empty black squares.[64,66,90,102,114,119,145] The experimental data corresponding to the Mg$_2$Si$_{1-x}$Sn$_x$ case are represented by solid blue circles,[41,47,48,87,92,99,112,144] while theoretical data by empty blue circles.[73,87,90,102,115,119] And, in the Mg$_2$Ge$_{1-x}$Sn$_x$ case, the experimental data is represented by solid red triangles,[47,112,146] while theoretical by empty red triangles.[64,71,102,145] Figure taken from reference [E1].

third order polynomial equation of the kind

$$p(x) = a_1(1-x) + a_2 x + \alpha x(1-x)^2 + \beta x^2(1-x), \qquad (3.5)$$

within an uncertainty of the order of 0.01% with respect to pure materials' data: $a_1 = p(x = 0)$ corresponds to Mg_2X and $a_2 = p(x = 1)$ corresponds to Mg_2Y. In that case, I only need to find two parameters to completely determine the trend: α and β. In fig. 3.4 I also compare my computations with other theoretical and experimental data, in all cases. Due to LDA I observe a typical underestimation of the lattice constant in comparison to experimental data as well as calculations using GGA.[119] The intermediate available theoretical data of the $Mg_2Ge_{1-x}Sn$ system is rather scarce, most of the data in this case exist in the pure material's limit. I also observe that, besides the deviations due to the LDA, the present calculations reproduce very well the experimental data.

Using the fitting parameters of the third order polynomial, I obtain the quadratic ($\beta - 2\alpha$) and cubic ($\alpha - \beta$) contributions to the trends. In the particular case of the $Mg_2Si_{1-x}Ge_x$ system, I see, from the values reported in the table 3.2, that the quadratic (0.03 Å) and cubic (0.012 Å) terms are small and thus can be roughly approximated by Vegard's law. This can be understood from the fact that Mg_2Si and Mg_2Ge have similar binding energies, similar nature of the band gap, and therefore for small variations of the lattice constant I expect for the Vegard's law to hold. In the remaining systems, from Mg_2X (X=Si, Ge) to Mg_2Sn, the inversion of the bands reduce dramatically the band gap and binding energies, thus increasing the difference in lattice constants and leading to larger non-linear contributions.

I take these structural outcomes as the input values for computing all BSFs for the intermediate systems. I observe also non-linear trends in the direct band gap (E_D), as presented in the top row of fig. 3.5, except in the $Mg_2Si_{1-x}Ge_x$ case that can be linearly fitted. My calculations are compared to theoretical and experimental data as well.[56,65,67,69,72,147] In the non-linear cases, I use a similar cubic polynomial of the form of eq. (3.5) to fit the data, where a_1 corresponds to the energy gap for the $x = 0$ composition, while a_2 corresponds to the gap of the $x = 1$ composition. Therefore, the numerical fitting gives the α and β parameters in energy (eV) units. In all cases, the SO splitting energy increases linearly with the substitution of a heavier Y element. A collection of calculations of pure material's and intermediate alloys' data is given in table 3.2.

The dramatically underestimated indirect band gap values E_I have been shifted by ~ 0.8 eV to fit the experimental data, as presented in bottom row of fig. 3.5. I observe a nearly constant trend for E_I in the case of $Mg_2Si_{1-x}Sn_x$, supported by experiments,[42,81] and also LDA and
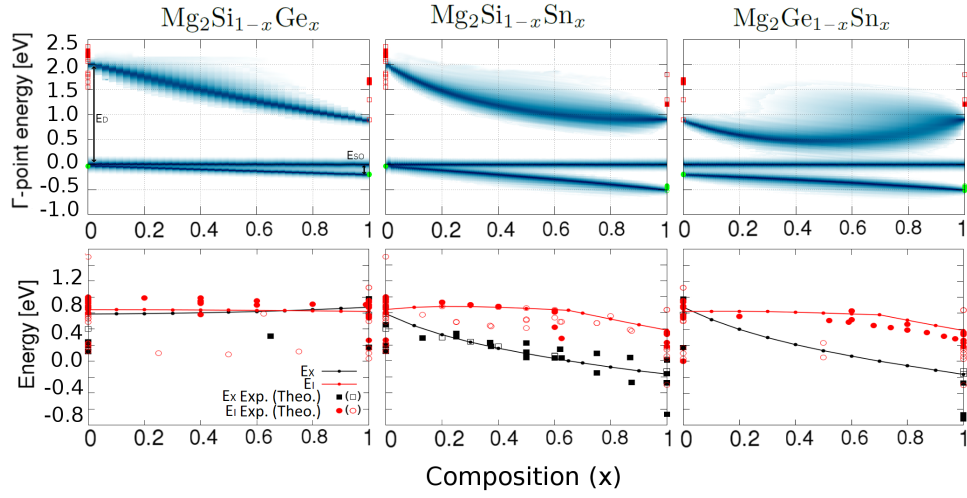
FIGURE 3.5: Top row: Calculations of direct band gap (E_D) and spin-orbit splitting (E_{SO}) energies at the Γ ($k = 0$)-point. The E_D experimental data is represented by solid red squares,[52,56], while theoretical values by empty red squares.[65,67,69,72,93,124,147] The SO experimental data is shown using solid green circles,[54,70] and theoretical data using empty green circles.[70,73,85] Bottom row: Shifted indirect $\Gamma - X$ band gap (E_I) and energy distance between the lowest-lying conduction bands (E_X), as function of the composition for all quasi-binary alloys. Experimental data of E_I are represented by solid red circles,[40,42,43,47–49,53,54,56,58,59,81] while theoretical data by empty red circles.[64,65,67,69,72,73,80,82,92,93,99,102,145,148] The experimental values of E_X are shown in solid black squares,[43,86,95,149] while theoretical data in empty black squares.[65,67,73,90,99,114,115] Figure taken from reference [E1].

corrected GGA theoretical values.[80,99] In the $Mg_2Si_{1-x}Sn_x$ case, I observe a constant non-linear reduction of E_X, that crosses $E_X = 0$ at $x = 0.6$, consistently with experiments[43,149] and other calculations.[90,114,115] The inversion of the bands is observed in the discontinuity of the slope in the E_I line, that decreases faster as $x \geq 0.6$.[65,77,92,148] In the last case, $Mg_2Ge_{1-x}Sn_x$, no comparative data is available for E_X at intermediate points, I only observe a slight overestimation in Mg_2Sn compared to experiments,[67,73] and a crossing of $E_X = 0$ at $x = 0.65$. This crossover is also evidenced in the E_I plot, and also agrees very well with experiments.[44,47,146]

3.1.6 Parabolic Band Effective Mass Approximation

3.1.6.1 Valence Bands

In the ideal case of quasi-free electronic states, the band structure can be locally modeled by a parabola and represented by a dispersion relation
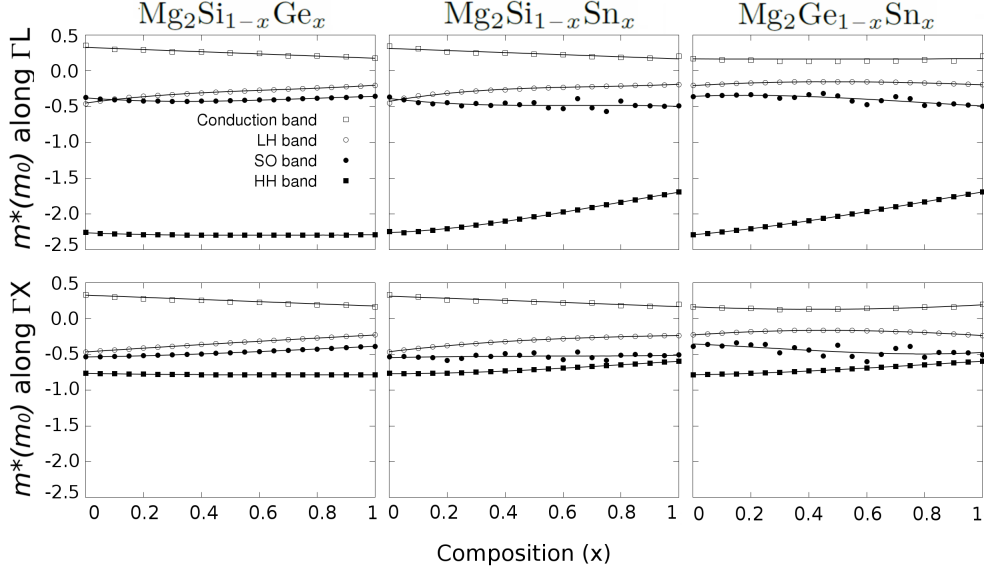
FIGURE 3.6: Effective mass calculations in the SPB approximation for the conduction and valence bands at the Γ point in the BZ of the quasi-binary $Mg_2X_{1-x}Y_x$ alloys systems, along different paths. Figure taken from reference [E1].

as $E(k) = E(0) + \hbar^2 k^2/2m^*$, where E, $\hbar$, k and m^* are the energy of electron states, the reduced Planck constant, the crystal momentum and the band effective mass, respectively.[62] However, I consider the SPB model more general by allowing different effective masses along different crystallographic directions. As shown in the schematic band structure of fig. 3.1, the HH and LH bands are locally degenerate at the Γ point, and then they become more dispersive and non-degenerate. As indicated above, the parabolicity range is valid up to $k \approx 0.03(2\pi/a)$ as long as non-parabolic contributions are negligible.[138] Using dense meshes along a particular k-path, and using a Lorentzian profile to fit the BSF maximum, I can find the effective mass parameters with the inverse of the parabolic curvature,

$$m^* = \hbar^2 \left(\partial^2 E(\mathbf{k})/\partial k^2 \right)^{-1}.$$

The resulting mass is given in units of the free electron's mass m_0. I have computed the corresponding band- and direction-dependent effective masses in the nearly pure crystalline limit of the Mg_2X materials, along the $\Gamma - L$ and $\Gamma - X$ directions in reciprocal space, for the conduction, LH, SO and HH bands, and the results are shown in fig. 3.6, and the fitting parameters are listed in the table 3.2. It should be noted that experimental values of effective masses given in table 3.1 correspond to

spatial- and band-averaged values, so that, direction dependent effects on the effective masses must be observed in the limit of perfectly oriented crystalline samples. As well, *n*-type effective masses correspond to low-lying conduction bands, located at the *X*-point, but I provide here only the effective masses corresponding to the conduction and valence bands at the Γ-point, relevant for weakly doped *p*-type samples.

As pointed out before, HH and LH bands present low alloying effects and the calculated values can be satisfactorily fitted; all fitting parameters can be found in table 3.2. In the case of the SO and conduction bands the effective masses show numerical noise due to the strong broadening of the bands. The effect is pronounced in the cases of Mg$_2$X$_{1-x}$Sn$_x$ (X=Si, Ge). Nevertheless, I computed a trend that matches the $x = 0$ and $x = 1$ points. The conduction band effective masses are, in general, linearly decreasing except for Mg$_2$Ge$_{1-x}$Sn$_x$ along $\Gamma - X$, where a cubic formula fits better.

I obtain a general non-linear decrease in the valence bands effective mass as the composition of the heavier Y atom increases. I note that the LH band effective mass slightly decreases in all cases, specially in the case of Mg$_2$Si$_{1-x}$Sn$_x$, as it was already reported.[73] The HH effective masses show a strong direction dependence and, away from the principal axes, the effective mass is increased by a factor of 2.9. I observe nearly constant HH bands masses in the case of Mg$_2$Si$_{1-x}$Ge$_x$, while monotonically decreasing in the remaining alloy systems. The LH band shows also a systematic non-linear decrease as the composition of the heavier Y increases but remaining nearly constant in the Mg$_2$Ge$_{1-x}$Sn$_x$ case. So I can say that the HH and LH bands, which are the most relevant bands in *p*-type transport, can satisfactorily be mapped on a SPB model. Thus my results provide valuable information about the band structure changes between pure Mg$_2$X materials.

3.1.6.2 Low-lying Conduction Bands

As I have already observed in the direction-dependent effective masses of valence and conduction bands at the Γ-point, I similarly assume a direction dependent effective mass model for the bottom of the conduction bands. I perform similar parabolicity tests on these bands and, as shown in fig. 3.7, I assume this parabolicity to hold up to nearly $k = 0.05(2\pi/a)$, or $\Delta E \approx 0.1$ eV.[120] In fig. 3.7 I present the conduction bands of Mg$_2$Ge$_{1-x}$Sn$_x$ that show similar features near the crossing point of bands ($x = 0.7$) as the Mg$_2$Si$_{1-x}$Sn$_x$ alloys near the crossing at $x = 0.65$. These bands are labeled as *light-* and *heavy*-conduction bands according to their

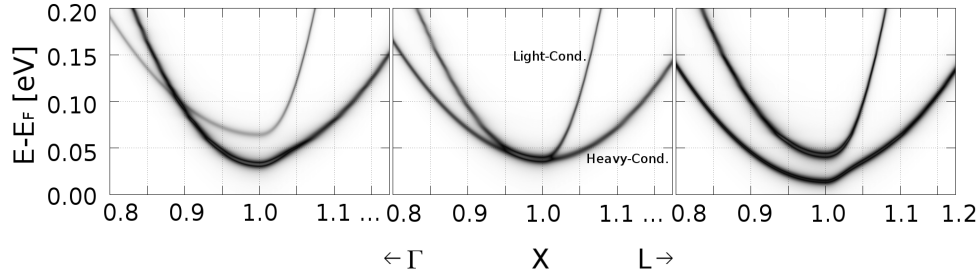**FIGURE 3.7:** Low-lying light- and heavy-conduction bands of $Mg_2Ge_{1-x}Sn_x$ at compositions near the crossing, $x = 0.65$ (left), $x = 0.7$ (center), and $x = 0.75$ (right), in the vicinity of the X-point [100] along $X - \Gamma$ and $X - L$, with k in units of $2\pi/a$ (dark gray corresponds to high BSF in a.u.). Figure taken from reference [E2].
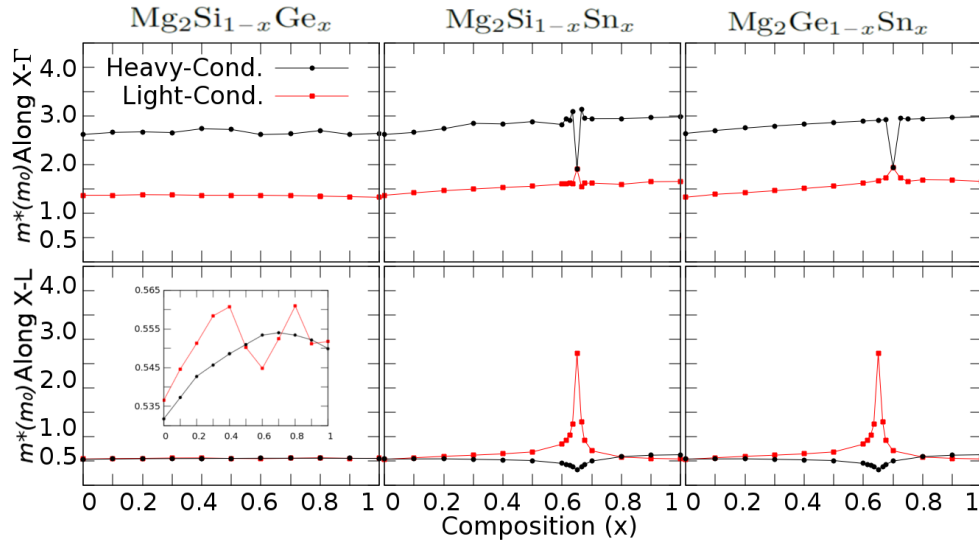

FIGURE 3.8: Parabolic band effective mass calculations corresponding to $Mg_2Si_{1-x}Ge_x$ (top), $Mg_2Si_{1-x}Sn_x$ (center), and $Mg_2Ge_{1-x}Sn_x$ (bottom), along the $X - \Gamma$ and $X - L$ directions, as function of the composition x. Figure taken from reference [E2].

local curvature, but this curvature is direction dependent as I will show below. I also observe that the degeneracy of the bands is larger along the $X - \Gamma$ direction, up to nearly $\sim 0.05(2\pi/a)$, than along $X - L$, where the degeneracy is only up to nearly $\sim 0.01(2\pi/a)$.

From the local band structure of the low-lying conduction bands of intermediate Mg_2X alloys, presented in fig. 3.7, I want to point out some interesting features. The light- and heavy-conduction bands cross at a k value below the X-point for compositions x smaller than that of the crossing point, i.e., $x = 0.65$ for $Mg_2Si_{1-x}Sn_x$ and $x = 0.7$ for $Mg_2Ge_{1-x}Sn_x$. This crossing increases with the unit cell volume,

controlled by the substitution of Sn,[104] and reaches its maximum when both electron pockets degenerate. In the $\Gamma - X - L$ path, I do not observe the crossing any more for compositions above the crossing point. This means that the crossing of the bands is direction dependent, and that the bands preserve their order in energy along the $X - L$ direction.

The characteristics of the low-lying conduction bands can be seen in the calculations of the effective masses, which I present in fig. 3.8. In the left column of this figure I show the $Mg_2Si_{1-x}Ge_x$ system, in which the heavy- and light-conduction bands are nearly constant and also manifest strong anisotropies. The bands effective masses along the $X - L$ direction are also nearly constant at $m \approx 0.5m_0$, but the zoom-in (inset) shows that light- and heavy-labels are indeed direction dependent, and also some noise is present in the light-conduction band due to alloying effects.

In the $Mg_2X_{1-x}Sn_x$ systems, I observe also that the effective masses are nearly constant except in the vicinity of the crossing point. As mentioned, I do not distinguish the bands along $X - \Gamma$, so their effective masses coincide at $x = 0.65$ for $Mg_2Si_{1-x}Sn_x$ and 0.7 for $Mg_2Ge_{1-x}Sn_x$, while along $X - L$ the light-conduction effective mass is sharply increased by nearly 5 times and the heavy-conduction band effective mass slightly decreases. From fig. 3.7, I can see that for higher energies, or k-values, these crossing effects should disappear and the trends of their effective masses should be monotonic. Experiments have revealed an enhancement of the thermoelectric performance in these materials, and this fact has also been corroborated by density of state (DOS) effective masses.[90,110,120]

3.1.7 Conclusions

Here, I describe the structural and electronic properties of the intermediate compositions of $Mg_2X_{1-x}Y_x$, for X = Si, Ge, Sn in the entire compositional range $0 \leq x \leq 1$. Within the KKR-CPA formalism in full-relativistic approach, I was able to obtain total energies and therefore the formation enthalpy to fit an equation of state and extract relevant structural parameters, such as the minimal formation energy and the equilibrium lattice constant. I regard these results as an approximation since the KKR-CPA ignores the ion-ion interaction and therefore the lattice dynamics. Consequently a complete relaxation of the system is still not possible. Nonetheless, this formalism is particularly powerful for the prediction of electronic properties such as band structures (or density of states), energy gaps - besides the shifts induced by the exchange-correlation potentials, and parabolic bands effective masses.

The complete solubility of $Mg_2Si_{1-x}Ge_x$ is explained from the relative

formation energy diagram, that shows no extra absorption or emission of energy compared to the end Mg_2X compounds. In contrast, the relative formation energy curve of the remaining $Mg_2X_{1-x}Sn_x$ lies above the energy of the binary compounds. This indicates that these intermediate compounds require more energy which might eventually released to decompose into the end compounds. These intermediate compounds have shown to be thermodynamically unstable.[80]

For intermediate compositions in all cases I compute the separation between the bands, or forbidden band gaps, in very good accordance with the experimental data, and accompanied with the systematic underestimations from DFT. In these systems, I have verified that the conduction bands strongly depend on the unit cell volume, controlled by the Sn content, and converge for $x = 0.65$ in $Mg_2Si_{1-x}Sn_x$ and $x = 0.7$ in $Mg_2Ge_{1-x}Sn_x$. This fact leads to a substantial increase in the effective masses as seen in section 3.1.6.2. Whilst the valence bands effective masses show a regular and monotonic behavior, the conduction bands effective masses show a peak in the composition of the crossing, except in the $Mg_2Si_{1-x}Ge_x$ system. I also noted that some of the bands are more affected by alloying effects than others. Thus, they are not well defined along $\mathbf{k}$, and therefore the computation of these bands are not easy to interpret.

3.2 Raman Scattering in Graphene

In this section I present an introduction to *inelastic scattering of light* - or *Raman scattering* (RS) - in material systems, with focus on graphene. I describe a theoretical approach to radiation-matter interaction in quantum systems. With this basis, I develop a quasi-phenomenological model for the Raman peaks using Lorentzian functions. These peaks resonate at the phonon frequencies *allowed* by conservation rules. The peak shape modeling allows me to study the phonon confinement effects that explain the frequency shift of the Raman peaks measured in micro-crystalline samples.

For the determination of the Raman frequency shift in graphene I compute the allowed phonons at different excitation energies using $1D$-DFT bands. For varying sample sizes, I compute the Raman peaks and study the additional shifts induced by the breakdown of the crystal symmetries and therefore the conservation laws. The results that I present reproduce the experimental data obtained within the research group of Prof. Dr. Klar very well.

In this study I do not present a $2D$ solution from the DFT calculations, due to the large and expensive requirements. I rather introduce an approximate tight-binding approach to the electronic and phonon bands that can be easily integrated in the full BZ of graphene, and allows me to interpret the results obtained using DFT calculations.

3.2.1 Introduction

RS has become a robust method for exploring the quantum properties of materials via the radiation-matter interaction. After nearly a century after its prediction and observation,[150,151] RS comprises an intense research field driven by improvements of the experimental equipment and theoretical models. Ordinary RS, or Raman spectroscopy, is a non-destructive technique used to obtain information about electronic and vibrational properties of materials such as crystals, molecules, liquids, etc.[152] This information is contained in the frequency shift, the k-vector (**k**) or the wave-length (λ) and the polarization (**e**) of the scattered light. Therefore, the basic approach is to observe the inelastic scattering of incoming laser light by molecular vibrations via outgoing light, and its spectral distribution. The latter reveals the Raman modes and their corresponding line shape properties.

A Raman process involves a change between initial and final states of a material system and the exchange of energy with the radiation field.

This radiation field may in general either transfer energy into the system, in the so-called *Stokes* process, or receive energy from it in the *anti-Stoke* process. This last case can occur only when the system is excited.

Within a macroscopic description, an incoming photon of frequency ω_i ($\mathbf{k}_i \lambda_i$), and polarization $\mathbf{e}_i$, which will be scattered into an outgoing photon of frequency ω_S ($\mathbf{k}_S \lambda_S$), with polarization $\mathbf{e}_S$, leaving behind the material system in an excited state of energy, is called Stokes RS. The scattered intensity I_S must therefore depend on $\mathbf{e}_i$, $\mathbf{e}_S$, and the atomic displacements and their effect on the variation of the electric susceptibility. Thus, the intensity I_S must contain all the information of the allowed and forbidden Raman processes, or the *Raman selection rules*, computed using a relation of the kind $I_S \propto |\mathbf{e}_i \cdot \mathcal{R} \cdot \mathbf{e}_S|^2$, with $\mathcal{R}$ as the Raman tensor.[153] A complete solution to the problem, using classical electromagnetism, demands an integration over the incoming/outgoing directions in order to find the possible resonances.

Using modern theoretical techniques, RS processes can also be obtained diagrammatically, or perturbatively, using Feynman diagram formalism.[152,153] Diagramatic methods allow one to obtain the possible contributions to the total Raman signal that involve high-order interactions, such as the electron-phonon interaction, multi-phonon interactions, radiation-phonon interactions, and so on. This method allows one to study inherent interference effects between different processes that can simultaneously cancel each other, and the selection rules are inherent to the formalism.

A quantum mechanical description of the Raman scattering process requires the Hamiltonian representation of the material system, the radiation field, and some interaction terms. The Hamiltonian of the material is, certainly, dependent on the material, with an energy spectrum of E_n excited states, the material is usually assumed to be in the ground-state $E_0 = 0$. The interaction term must describe the coupling between the material and photons with some quantum numbers: wave-vector, polarization mode, polarization vector, and angular frequency. Moreover, some extra terms must be included in the model Hamiltonian for completeness, e.g., electron-electron interactions, nuclear motion, spin to describe magnetic properties, etc.

In this description, the Raman cross section can be approximated by a golden rule-like equation of the form,[153]

$$\mathcal{M} \sim \sum_{s_0, s_1, \ldots, s_n} \frac{\langle i| \hat{H}_{e-em} |s_0\rangle \ldots \langle s_{n-1}| \hat{H}_{e-ph} |s_n\rangle \langle s_n| \hat{H}_{e-em} |f\rangle}{(E_i - E_0 + 2i\gamma)(E_i - E_1 + 2i\gamma) \ldots (E_i - E_n + 2i\gamma)},$$

(3.6)

where i and f denote the initial and final state of the system, and the $\hat{H}$ terms correspond to the electron-radiation field ($e - em$) and electron-phonon ($e - ph$) interaction Hamiltonians. The sum is performed over all possible processes, in which an incoming photon with energy E_i must match the electron/hole energy difference at $\mathbf{k}_i$, and then the interaction with the phonon $\mathbf{q}_0$ with energy $\omega(\mathbf{q}_0)$. The resonances are found for those possible pairs $(\mathbf{q}_0, \omega(\mathbf{q}_0))$ that minimize the denominator of eq. (3.6); in this equation, γ represents the life time of the intermediate states. Therefore, the Raman intensity yields its resonance at the Raman *allowed* active modes $\mathbf{q}_0$. The states of the system, represented by the bra-kets in eq. (3.6), are in principle separable even in the case of electrons and phonons due to the Born-Oppenheimer approximation. In that case, the electron-phonon coupling is treated as a perturbation and the states of the system, without the radiation field, can be regarded as static; therefore, it is in principle a good approximation to treat these states using the eigen-values of the system obtained by *ab initio* methods. The radiation field can then excite, independently, either an electronic or phonon quantum state of the system or a coupled electron-phonon state in a more complicated process.

Note that the imaginary part of eq. (3.6) can indeed be approximated by a real-valued Lorentz function, or a product of such a functions for the Raman active modes, and that the complete Raman peak shall vanish for all energies except those at resonance.

In the lowest order of scattering, the fundamental Raman selection rule reads $q_0 \approx 0$, and comes from the fact that the photon wave vector is nearly negligible and all unit cells must vibrate with the same phase. This scattering mode measures the phonons in the vicinity of the Γ point ($\omega(0)$). Higher-order multiple-phonon ($q_0 = q_1, q_2, ...$) interactions are also Raman active as overtones under the condition that $\sum q \approx 0$.

There is a particular interest in the resonant Raman processes in which the excitation of the incident phonon involves real electronic states. Single incoming and outgoing resonances in Raman spectroscopy occur if the energy of the incoming or the scattered photon matches the transition of allowed electronic states leading to a large enhancement of the Raman cross section.[152] Double-resonant Raman scattering involves two real electronic transitions and can also occur in parabolic semiconductors, or in semi-metals like graphene. If the sample contains symmetry breaking elements, they relax the quasi-momentum conservation and its dispersion is used to probe the phonon or electronic structure at vectors away from the Γ point.[154]

3.2.2 Raman Peaks Modeling: Confinement of Phonons in micro-Crystalline Samples

The Raman active phonon modes, $\omega(\mathbf{q}_0)$, that resonate in the Raman intensity eq. (3.6), must satisfy the physical conservation laws for energy and momentum that correspond to the symmetries of the system. However, for symmetry breaking elements, such as defects and boundaries in the material system, these selection rules do not hold anymore and $\mathbf{q}_0$ is not a good quantum number any more. The Lorentzian line-shapes, centered at $\mathbf{q}_0$, are then broadened indicating that the transition probability is non-vanishing for neighboring phonon modes, apart from $\mathbf{q}_0$.

To describe quantum confinement of phonons, a phenomenological model has been proposed that describes the line-shape changes of the Raman intensity as a function of the size of the sample and the excitation energy of the radiation field. This means that the observed Raman shifts due to the micro-crystalline effects are well described, except the amplitude decay observed in bulk materials. As the size of the crystals reduce, different phonons around $\mathbf{q}_0$ must contribute to the scattering processes weighted by a confinement function.[155,156]

The starting point is to define a phonon wave-function for the active Raman mode $\omega(\mathbf{q}_0)$, in the crystal limit, expressed as

$$\phi(\mathbf{q}_0, \mathbf{r}) = u(\mathbf{q}_0, \mathbf{r})e^{-i\mathbf{q}_0 \cdot \mathbf{r}}, \tag{3.7}$$

where $u(\mathbf{q}_0, \mathbf{r})$ has the periodicity of the lattice. The phonon confined to a micro-crystal of diameter L must be of the form

$$\psi(\mathbf{q}_0, \mathbf{r}) = W(\mathbf{r}, L)\phi(\mathbf{q}_0, \mathbf{r}) \equiv \psi'(\mathbf{q}_0, \mathbf{r})u(\mathbf{q}_0, \mathbf{r}), \tag{3.8}$$

where $W(\mathbf{r}, L)$ is a generic confining weight-function, such that, in the limit $L \rightarrow \infty$, one recovers the crystal-limit wave function eq. (3.7). Note that this weight-function must be system dependent and must also account for its symmetries. Here I will retain a Gaussian representation of this function, written as

$$W(\mathbf{r}, L) = A \exp\left\{-\frac{r^2}{2}\Big/\left(\frac{L}{2}\right)^2\right\}, \tag{3.9}$$

since I assume that the boundaries of the sample, suspended over an elastic substrate, are allowed to move. Note that eq. (3.9) is an isotropic function and its functional form does not depend on the dimension.

Another choice of the weight-function, such as a step-like function or the lowest Bessel function with rigid boundaries, will induce spurious contributions to the Fourier transform not observed experimentally.

The Fourier transform of ψ' is given by

$$\psi'(\mathbf{q}_0, \mathbf{r}) = \int d^3 q \, C(\mathbf{q}_0, \mathbf{q}) e^{i\mathbf{q}\cdot\mathbf{r}}, \qquad (3.10)$$

with Fourier coefficients given by

$$C(\mathbf{q}_0, \mathbf{q}) = \frac{1}{(2\pi)^3} \int d^3 r \, \psi'(\mathbf{q}_0, \mathbf{r}) e^{-i\mathbf{q}\cdot\mathbf{r}}. \qquad (3.11)$$

Inserting eq. (3.8) and eq. (3.9) in eq. (3.11), I find

$$C(\mathbf{q}_0, \mathbf{q}) = \frac{AL}{(2\pi)^{3/2}} \exp\left\{ -\frac{1}{2} \left(\frac{L}{2} \right)^2 (\mathbf{q} - \mathbf{q}_0)^2 \right\}. \qquad (3.12)$$

This generic description is made for a $3D$ system and the integration constants are strongly dependent on the dimension. I carefully employ this model in the case of $2D$ graphene and also for $1D$ DFT bands with a corresponding change of the proportionality constant.

The wave-function ψ' is no longer an eigenfunction of the phonon wave-vector $\mathbf{q}_0$ but rather a superposition of $\mathbf{q}$-values around $\mathbf{q}_0$ weighted by the decaying Gaussian function eq. (3.12), in a range of the order of $|\mathbf{q} - \mathbf{q}_0| \leq 1/2L$. This implies that the transition matrix elements from $\mathbf{q}_0$ to $\mathbf{q}$, mediated by the photon-phonon interaction operator, are non-vanishing for $\mathbf{q} \neq \mathbf{q}_0$ and therefore momentum is no longer conserved.

Now, as I have presented in the introduction, the Raman peak profile given by eq. (3.6) can be approximated by a Lorentzian function, and this function is the usual approach for fitting peaks in Raman analysis. For any confined phonon at $\mathbf{q}_0$, the Raman intensity peak is written as

$$I(\omega) \approx \int \left| C(\mathbf{q}, \mathbf{q}_0) \right|^2 \mathcal{L}(\omega, \omega(\mathbf{q})) d\mathbf{q}, \qquad (3.13)$$

where $\omega(\mathbf{q})$ is the phonon frequencies and the integration is performed in the first (or reduced) BZ. In eq. (3.13), the Lorentzian function $\mathcal{L}$ is given by

$$\mathcal{L}(\omega, \omega(\mathbf{q})) = \frac{\Gamma/\pi}{(\omega - \omega(\mathbf{q}))^2 + (\Gamma/2)^2}, \qquad (3.14)$$

with Γ as the full-width at half-maximum (*FWHM*) that I will conveniently assume as constant.[157] In the crystalline limit, I have $C(q_0, q; L \rightarrow \infty) \rightarrow \delta(q - q_0)$, with $\delta(x)$ as the Dirac delta distribution, and for two dimensions I use the property $\delta(\mathbf{r} - \mathbf{r}_0) = \delta(r_x - r_{0x})\delta(r_y - r_{0y})$.

3.2.3 RS in Graphene

RS has shown to be a very powerful and non-destructive technique to characterize carbon-based materials, such as graphite, since it is sensitive to its atomic properties, such as the number of layers, doping, disorder, crystalline size, electron-phonon coupling, and its mechanical properties. Graphite consists of a collection of 2-dimensional (2D) hexagonal arrays of sp^2-carbon atoms, or *graphene* sheets, separated by an inter-layer distance $\sim 3.4 - 3.7$ Å. The inter-layer distance is larger than the covalent bond distance of the intra-layer carbon atoms, ~ 1.42 Å, as illustrated in fig. 3.9.[158] The lattice sites of graphite correspond to the space group $P6_3/mmc(= D_{6h}^4)$, while those of graphene correspond to D_{6h}. The building-block of graphite, graphene, contains two atoms in its unit cell, A and B, that can vibrate in- and out-of-plane in the direction shown in the unit cell illustrated in the right part of fig. 3.9. Correspondingly, the first BZ is composed by two inequivalent K-valleys, as shown in fig. 3.10.
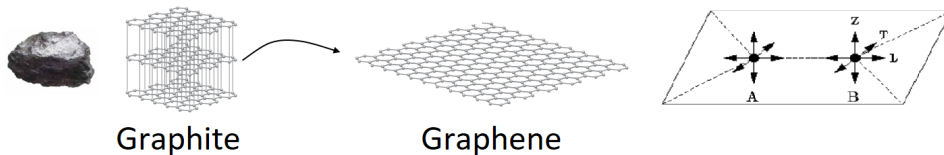
Graphite   Graphene

FIGURE 3.9: (left) Graphite, multiple stacked hexagonal layers of sp^2 carbon atoms - graphene - (center), with two atoms in the unit cell (right). Both atoms can vibrate either in-plane (T or L), or out-of-plane along Z. Figure adapted from `http://phelafel.technion.ac.il/~tzipora/`

Early measurements of the Raman spectra in graphite revealed a strong peak at ~ 1580 cm^{-1}, nowadays known as the G peak, as shown in fig. 3.11.[159,160] This frequency has been assigned to the in-plane Raman active and degenerate E_{2g} phonon modes present in graphene, though the inter-layer interaction slightly splits this degeneracy in graphite. This peak corresponds to a robust reference peak to measure and compare
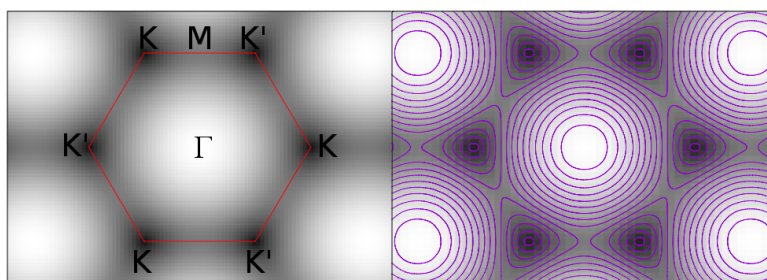
FIGURE 3.10: Computed Hexagonal Brillouin zone of graphene and a contour plot of the conduction band using the TB electronic bands.[158] The high-symmetry points Γ, *K* and *M* are indicated.
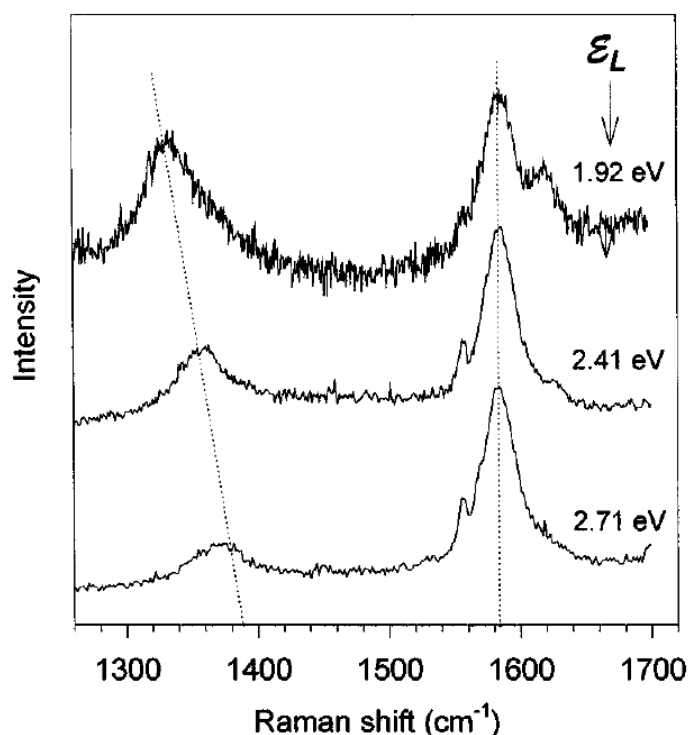

FIGURE 3.11: Raman spectrum of sp^2-based carbon polyparaphenylene (PPP) at 2400 °C. Figure taken from literature.[159]

other peaks present in the Raman spectra of graphite. Moreover, this peak has been extensively studied and has been seen to evolve from a single-peak in graphene to a wider peak in graphite, composed of multiple contributions at different phonon frequencies.[161,162]

Below this frequency, between $1300 - 1400$ cm^{-1}, another Raman line has appeared in the spectrum for defect or micro-crystalline samples, with an intensity that inversely depends on the crystalline size, and is not present in nearly pure crystals.[159] This, so-called defect-induced *D*

mode, was not completely understood in the beginning; it was actually attributed to a diamond-like formation in the sp^2 rings and chains.[160] This *D* Raman peak has shown to be strongly dispersive with the excitation laser energy, but this behavior is essentially the same irrespective to the carbon (sp^2) sample.[163] The integrated frequency of this band shifts down by ~ 30 cm^{-1} when the laser wavelength increases from 488 to 647 nm,[164] i.e., the frequency varies approx. $40 - 50$ cm^{-1}/eV, while the intensity decreases with increasing the laser energy.[165,166] For small samples, a shift of 15 cm^{-1} has been observed in the *G* peak toward higher wave-numbers due to a breaking of the symmetry of the system and therefore a broadening of the possible phonons involved around the Γ point.

Since no Γ-point phonons exist at all in the frequency range of the *D* peak, the behavior of this band obey some special **k**-selection rules. Only phonons near the *K*-point, the BZ boundary, not present in the usual first-order Raman process, could explain the Raman spectra. However, in a first-order Raman process, such a violation of the *k*-conservation is possible in disordered materials only. It was proposed, that this peak comes from a double-resonant process that involves the interaction of two real electronic transitions and one phonon. This idea was proposed nearly 20 years after the first experimental evidence of this peak.[167] This model assumes that the phonons involved in such an interaction must lie in the neighborhood of the inequivalent *K*-points of the graphene BZ, shown in fig. 3.10. Therefore, this defect-induced peak allows the measurement of phonon modes in a wider region of the BZ, away from the Γ point.[154,161] The origin of the *D*-mode in graphite and C-nanotubes is similarly well established as being defect-induced double resonant scattering.[168]

A complete solution to the double-resonant problem in graphene consist of a $2D$ integration, in the reciprocal space, of the Raman scattering cross section given by eq. (3.6) considering a reasonable expansion of the possible interactions.[169] My approach will be rather different. Instead of a complete diagramatic solution to the problem, I will adopt a quasi-intuitive approach that considers the possible inter- and intra-band ($\pi^* \rightarrow \pi$ or $\pi \rightarrow \pi$) dispersion in the inter-valley ($K \rightarrow K'$) case, to explain the experimental results of the *D* mode in graphene. For this purpose, I will rely on the details of the electronic and phonon structures using DFT techniques in $1D$ along the symmetry points of its BZ. The DFT electronic and phonon bands, as presented in fig. 3.12, have been obtained using the Quantum ESPRESSO software package,[170,171]. I relaxed the structure and the obtained lattice parameters lie $\sim 0.01\%$

below the experimental value. I set the out-of-plane (vacuum) distance to be $c/a \approx 1.2$, where a is the in-plane lattice constant.

I computed the electronic structure using a non-relativistic and ultrasoft pseudo-potential, and within the Perdew-Burke- and Ernzerhof (PBE) parametrization of the GGA for the exchange-correlation functional.[17] In the resulting electronic structure, as can be seen in fig. 3.12, I have found an underestimation of about 16% of the band gap at the M-point, where van-Hove singularities occur. Consequently, I have to re-scale the electronic bands in order to correctly describe the experimental data.[172] The valence (π) and conduction (π^*) bands of graphene cross each other at the K point, where they are nearly linear and symmetric. These bands have been extensively studied using tight-binding (TB) techniques up to high orders of approximation in the hopping parameters that allow to have analytical expressions of these bands.[158,173] I will use below these TB representations of the bands to analyze $2D$ effects on the Raman active modes. It is found, that around K these bands are homogeneous and symmetric, and effectively described by a massless fermion Weyl-Dirac equation, thereby the K points are also known as the *Dirac points*. This linearity holds for energies above the Fermi level to ~ 1 eV. Then these symmetric bands transform into trigonal bands in $2D$, as has been sketched in the right part of fig. 3.10.[174]
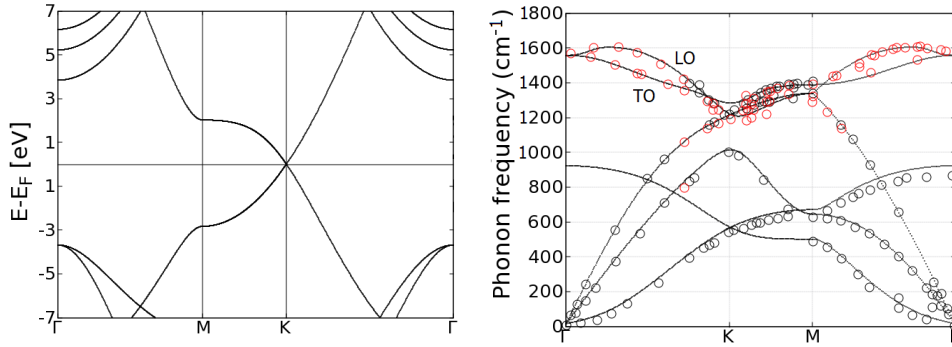
FIGURE 3.12: (left) Electronic $E(\mathbf{k})$ and (right) phonon $\omega(\mathbf{q})$ spectra of graphene, obtained using *ab initio* techniques. The calculations are represented by the solid lines while the experimental data of phonons, from literature, is shown using open circles.[175,176] The electronic structure is re-scaled to fit the experimental band gap.[172]

For the phonon structure I use the same input parameters as in the case of the electronic structure, as well as the same pseudo- and exchange-

correlation potential. The obtained phonon structure is presented in the right part of fig. 3.12, and is compared to available experimental data.[175,176] Using these parameters, I obtained a phonon dispersion with longitudinal-(LO) and transverse-optic (TO) bands slightly underestimated by $\sim$ 16 cm^{-1}, but a perpendicular-optical (ZO) band slightly overestimated, and not relevant for this work. Some other calculations show a general over-estimated phonon structure, as the results depend on the choice of the exchange-correlation potential.[177]

Since each unit cell in the graphene lattice contains 2 atoms and therefore 4 in-plane degrees of freedom, at the Γ point two acoustic and two optical modes are found and they are degenerate. Graphene has the following normal modes at Γ: A_{2u}, B_{2g}, E_{1u}, and E_{2g}. The A_{2u} and E_{1u} representations correspond to the translations of the plane; the B_{1g} mode is an optical phonon where the carbon atoms move perpendicular to the graphene planes. E_{2g} is the doubly degenerate in-plane optical vibration and is the only Raman active mode. At the Γ point, the in-plane polarized longitudinal- (LO) and transverse-optic (TO) modes are degenerate, but, as it has been already studied and demonstrated, only the TO band is Raman active. I also note that this band is approximately parabolic in the vicinity of the K point. The Raman fundamental rule to measure the G band involves a electron/hole pair creation by the incoming laser radiation that must be dispersed by a $q \approx 0$ phonon, followed by a recombination of the electron and hole. This situation is sketched in fig. 3.13, where it can be seen that this electronic transition is not necessarily resonant but the intermediate electronic state could be virtual; however, the peak is strongly enhanced as the transition reaches the resonant condition and this can be reached using, e.g., doping of graphene.

Besides these G and D peaks in the Raman spectrum of graphene, the so-called D' peak has also been found at 1620 cm^{-1}, and this transition is explained using a defect-induced inter-band and intra-valley dispersion, as shown in fig. 3.13. This last dispersion, in contrast to the D band, is always present since the electron/phonon recombination process can be also phonon-assisted. The strong peak at $\sim$ 2700 cm^{-1}, the G' peak, corresponds to the emission of two phonons with opposite wave vectors near the K ad K' points. Sometimes this peak is also denoted by $2D$ or by D^* to stress that it is the second overtone of the D peak.
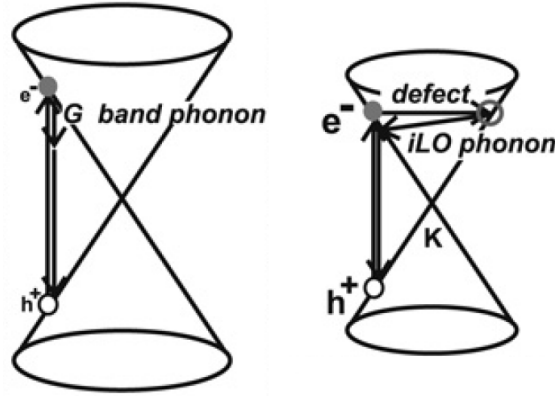
FIGURE 3.13: (left) Electron/hole pair creation for the $q \approx 0$ Raman funda-mental rule of the G mode. (Right) A defect-induced intra-band and intra-valley double-resonant dispersion with phonons near Γ.Figure taken and modified from literature.[178]

3.2.4 Dispersion of the Defect D Mode in $1D$: an *ab initio* Approach

To state the problem, let me consider the linear part of the electronic spectrum in the 2-dimensional space, i.e., for excitation energies below 2 eV, and not higher as is usually assumed in literature.[174] A resonant electron/hole excitation will require that the laser energy matches the energy difference between the valence and conduction bands with initial and final states, at P_1 and P_2 in fig. 3.14, with nearly the same k-vector. In this linear regime, for a given excitation energy $E_i \equiv E(k_i)$, there are two possible initial k_i-vectors that will be dispersed to $k_i + q_0 = k_f$ by a phonon q_0. For the inter-valley process, there are in total four q_0-vectors that satisfy the double-resonance condition. These vectors are given by $q_0 = 2K \pm (k_i \pm k_f)$, where q_0 is found using the conservation of the energy $\omega(q_0) = \pm(E_i - E_f)$ in a Stokes (+) or anti-Stokes (−) process. After this, the electronic state must be elastically back-scattered, e.g. by a defect, to a virtual state at k_i and then recombined with a hole to emit the outgoing photon.

This process can be in general more complicated, e.g., the phonon- and impurity-processes can occur at any order to contribute in the intensity given by eq. (3.6): the hole can be scattered as well, etc. But in either way, in order to annihilate radiatively in the recombination process, the electron and the hole must have opposite momenta and there are, in principle, infinite ways to fulfill the recombination condition. However, I will confine my discussion to the possible processes presented in fig. 3.14.

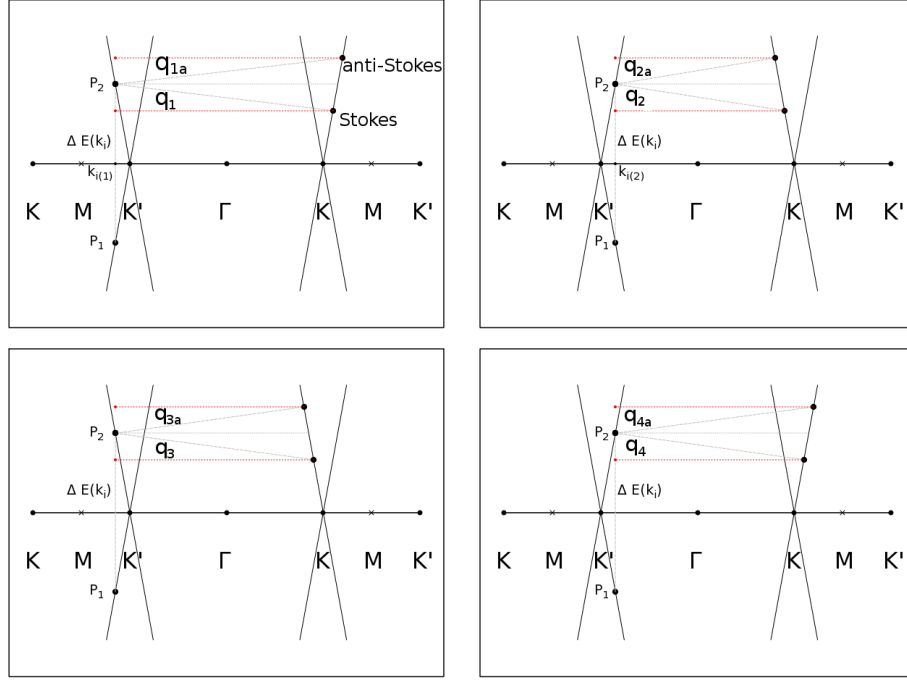For the process presented in the top-left part of fig. 3.14, $q_1 =$

FIGURE 3.14: Double resonant scattering process leading to the *D* mode in graphene.

$2K + (k_i + k_f)$ and $\omega(q_1) = E_i - E_f$, and q_1 belongs to the $K\Gamma$ path. Note that, for the anti-Stokes process, the expression for the q_{1a} value is identical, but the energy conservation requires that $\omega(q_{1A}) = E_f - E_i$. In the process of the top-right part of this figure, $q_2 = 2K - (k_i + k_f)$, and lies in the KM path. For the process of the bottom-left, $q_3 = 2K + (k_i - k_F)$, and for that of the bottom-right part, $q_4 = 2K - (k_i - k_f)$. The equation for the conservation of energy in these processes is the same and depends whether it is a Stokes or anti-Stokes process.

To illustrate this case, let us assume that the conduction and valence bands are symmetric and they meet at the Fermi level,[158] with a dispersion relation like $E(k) = \hbar v_F |k|$. Then the laser energy should be $E_{laser} = 2E(k) = 2\hbar v_F k$, for $k > 0$. Similarly, in the neighborhood of the K-point, the phonon dispersion can be approximated as a parabola of the sort $\omega(q) = \omega_0 + \alpha q^2$, with positive activation energy ω_0 and curvature α. In the Stokes or anti-Stokes process, the conservation of energy yields the same quadratic equation for the allowed q_0, $\hbar v_F q_0 = \omega_0 + \alpha q_0^2$, but I am only interested in the lowest solution. This means that, irrespective to the laser energy and the kind of process, there will be only one phonon combination $(q_0, \omega(q_0))$ that contributes to the Raman signal in this strictly symmetric case. In practice, these values are $q_0 = 0.0049(2\pi/a)$,
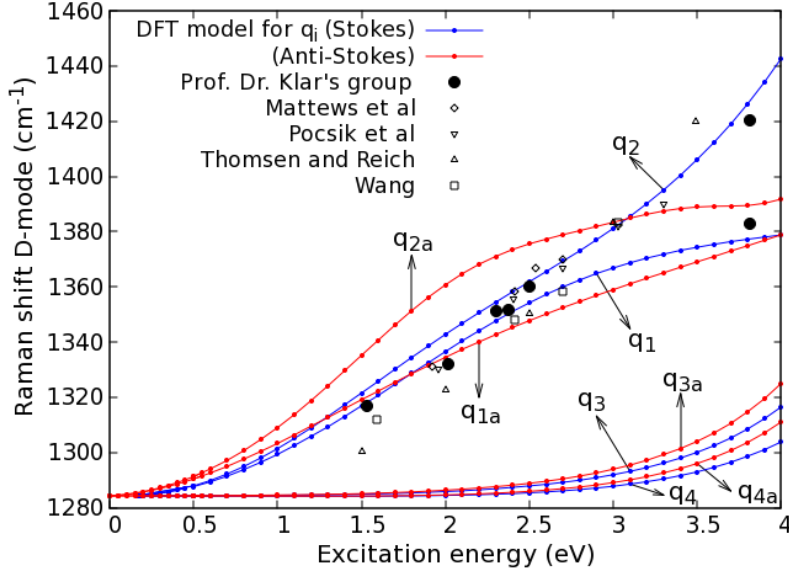
FIGURE 3.15: Computed frequencies of the *D* band as function of the excitation energy, compared to experimental data.[159,163,165,167]

away from $K^{(')}$, with energy $\omega(q_0) = 1269.26$ cm^{-1} (~ 0.157 eV).

To extend this study to the real non-linear and non-symmetric $1D$ case of graphene, I use the *DFT* bands presented in fig. 3.12 For each excitation energy there are still in general two available initial k-vectors, k_i, and for each of these, four q_0-vectors that matches the resonance conditions in either intra- or inter-band transitions, as illustrated in fig. 3.14. Note that the general expression for q_0 is $q_0 = 2K \pm (k_i \pm k_F)$, where the first $\pm$ stands for the path in the BZ, and the second relates to the inter- or intra-band process. The conservation of energy is given by $\omega(q_0) = \pm(E_i - E_f)$, where $\pm$ stands for the Stokes and anti-Stokes process, and E_f is the energy of the final k_f state. For all possible q-values I compute the Raman shift as presented in fig. 3.15. I observe that the inter-band Stokes q_1 and q_2 wave vectors reproduce very well the experimental data, and that the anti-Stokes curve lies above that of the Stokes process but only at low energies. All q-values converge at low energies, in the linear regime, as indicated above, and $E = 0$ is only possible in the anti-Stokes process.

Moreover, I observe that q_{3a} and q_{4a}, and the corresponding anti-Stokes q-values, are of magnitude close to K so that the resulting shift is negligible; the bands are nearly flat. These processes have been attributed to destructively interfere.[154] Stokes and anti-Stokes processes have also been measured in graphite[179] and CNs[157]. It has been generally argued that the anti-Stokes shift lies below that of the Stokes by an amount of

nearly $7 - 9$ cm^{-1},[180] but I only observe this behavior in a part of the excitation energy range. I noticed that the q_3 and q_4 are not observed in experiments, and the reason requires an extra term in the conservation rules, the conservation of the Fermi velocity. As I present below in the $2D$ TB analysis, if I consider solely the conservation of momentum and energy, several **q** vectors with moduli $\sim K$ participate in the Raman scattering process, but filtering those processes that preserve the Fermi velocity component yield the correct experimental Raman spectrum.

3.2.5 Micro-Crystaline Raman Shift of the G Band

As discussed, for the zone-center vector ($\mathbf{q}_0 = 0$), at Γ, the G-band is non-dispersive and has a value of ~ 1580 cm^{-1}. I compute a set of line shapes for different micro-crystalline sizes, using the Raman line shape functional profile given by eq. (3.13). Thus, I can show how these peaks deform as the size decreases, as can be seen in the left part of fig. 3.16. For small lengths, the neighboring phonons around q_0 contribute to the Raman peaks and shifts its mean - or weighted - frequency center to higher values reaching a maximum at ~ 4 nm. In the Γ point of the BZ of graphene there are two E_{2g} degenerate bands, as shown in fig. 3.12. Only the TO band, locally convex, is observed to contribute to the experimentally observed Raman shift of this band, as shown by the experimental values presented as well in fig. 3.16.
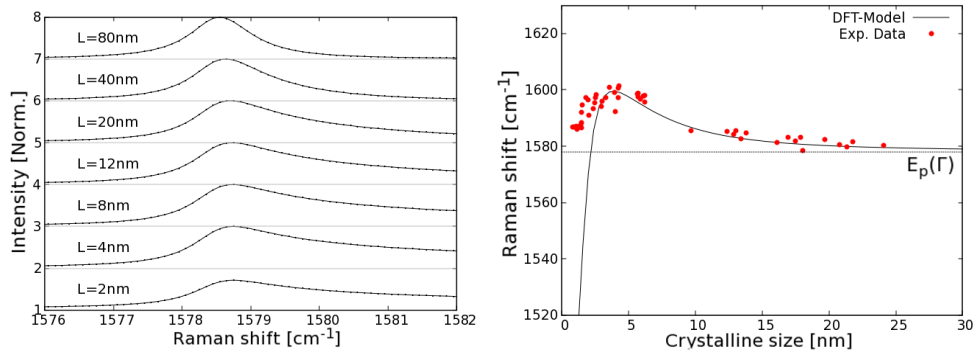
FIGURE 3.16: (Left) Raman line shapes of the G mode in graphene, obtained using eq. (3.13), for different crystalline sizes (L). (Right) Raman shift of this mode as function of the micro crystalline size.

In the right side of fig. 3.16, I present the integrated Raman shift frequency of the G-band of graphene, compared to experimental data

obtained in the group of Prof. Klar, and the Raman active mode E_g of crystalline graphene. I observe a very good agreement of the model compared to the experimental data in literature. They report an absolute shift $\sim 15 - 20$ cm^{-1} of the G mode.[165] However, I expect this model to fail at very low lengths as it predicts a negative shift due to the values of the TO band away from the Γ point.

3.2.6 Micro-Crystaline Raman Shift of the D Band

The case of the D band is similar to that of the G-mode, since the TO band is nearly parabolic and convex in the vicinity of the K or K' points as well. But instead of the zone-center vector, the D-mode takes place at $\mathbf{q}_0 \sim \mathbf{K}$. This band is strongly dependent on the local details of the electronic and phononic spectra and is accordingly strongly dispersed as has been shown in fig. 3.15. Therefore, in the $1D$ case, for a given energy, the Raman line shapes must deform around the corresponding values of q_0 (q_1 and q_2), but the deformation must be apparently similar to that of a generic locally parabolic band. As an example, I consider the Raman shape profiles of $q_0 \approx 1320$ cm^{-1}, with an excitation laser energy of $E = 1.57$ eV, presented in the left part of fig. 3.17 for different micro-crystalline sizes.
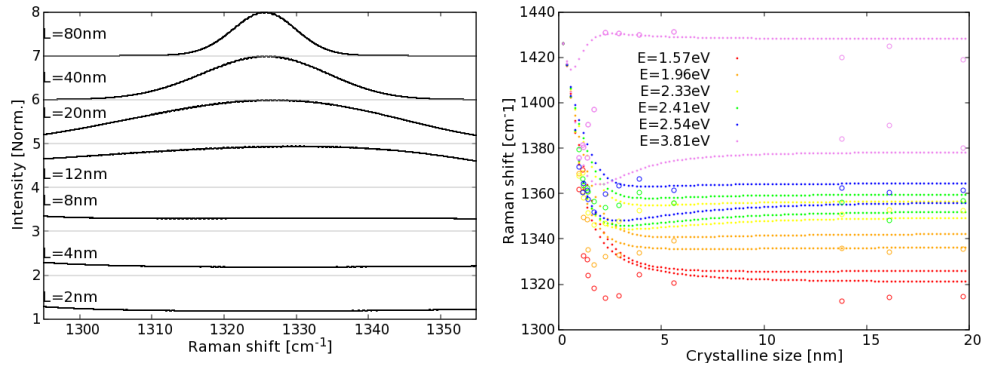
FIGURE 3.17: (left) Raman peaks of the D mode for different crystalline sizes, at $E_1 = 1.57$ eV. (Right) Raman shifts for different energies and lengths.

A direct computation of the integrated frequency yields the Raman shift of the peak as function of the sample diameter for different laser energies, as shown in the right part of fig. 3.17, where I also present the experimental data from Prof. Klar's group. In this plot, each color

represents a different laser excitation energy, in either the model or the experimental data, for the same energy values as those of the excitation energy of the *D*-band presented in fig. 3.15. It is worth to note, that the non-linear shift of the Raman bands reaches a plateau near 20 nm, where the shift value roughly corresponds to that of the crystal limit. This is not the case in the *G*-band that seems to be more sensitive to micro-crystalline effects at larger *L*. As in the last case, I do not trust completely the model as $L \to 0$, but away from that, the experimental trends are very well reproduced by the model.

3.2.7 The Intensity Ratio

The peak modeling given by eq. (3.13) reproduce very well the integrated frequency shift of the *D* and *G* bands in microcrystalline graphene, but does not considers the decay of the probability of scattering as $L \to \infty$. Therefore, I predict a constant Raman peak ratio for crystalline samples due to a constant density of defects. Additionally, the amplitude constant is somewhat arbitrary and therefore an intensity ratio between the *D* and the *G* peaks will tend to 1 for large sample sizes, as shown in fig. 3.18. The only differences that I observe are contained in a small window of the crystalline size as shown in the inset of fig. 3.18.
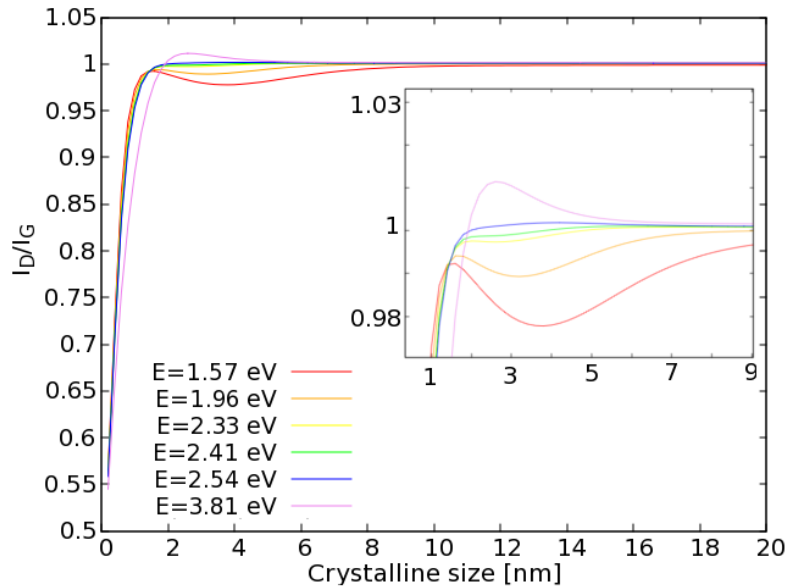
FIGURE 3.18: Intensity ratio between the *D*-mode and the *G*-mode peaks, I_D/I_G, as function of the crystalline size for different excitation energies.

In real samples the defects are mainly at the boundaries. Thus, the density of defects decreases with increasing the sample size leading to a decay of the ratio between the D and G modes. Consequently, in experiments the I_D/I_G ratio has been observed to have a maximum at ~ 2 nm and then decays as $1/L$.[160] This *phenomenological* decay has also been modeled to fit the so-called Tuinstra-Koenig formula of the sort $I_D/I_G = C(\alpha)/L$, where $C(\lambda)$ is a proportional constant that depends on the excitation laser energy.[181,182]

3.2.8 Tight-Binding Description of the D Band in $2D$ Graphene

Since the complete integration of the $2D$ problem in graphene requires a huge computational effort to obtain and interpolate detailed surface information, from the DFT point of view, I will try to illustrate the possible results using the TB approximation of the bands. The main problem consists of the construction of an algebraic representation of the electronic (and hole) and phonon (TO) bands that captures the important experimental physical parameters. A TB representation of the electronic bands has been exhaustively studied in literature in many orders of approximation.[158,173] Here, I will retain only the lowest order considering interactions only with the first nearest neighbors. For the phonon TO band I construct a surface function based on the electronic surface with the symmetries of graphene. This function must be locally parabolic at Γ and M, and nearly flat at K, and must cover the band-width given by the DFT data in fig. 3.12.

The comparison between the DFT and the resulting TB bands is presented in fig. 3.19 along the high-symmetry points. In the electronic part, I observe that both bands differ in the energy scale, though they have been prepared to coincide in the band-gap value at the M-point. Similarly, the TO phonon TB band present serious deviations from the DFT band but the overall shape is readily reproduced. Therefore, as an approximation for the energy range of our interest, I will present a complete $2D$ integration of the Raman D mode that depends on the excitation energy and the sample size, using these surface functions of the bands.

As in the $1D$ case, the general $2D$ problem consists of finding out the Raman active vectors $\mathbf{q}_0 = (q_{0x}, q_{0y})$ that disperse the iso-energetic $\mathbf{k} = (k_x, k_y)$ vectors, defined by $E(\mathbf{k})$, into a resonant $\mathbf{k}_f$ lying at the iso-energetic curve $E(\mathbf{k}_f)$, as illustrated in fig. 3.20.

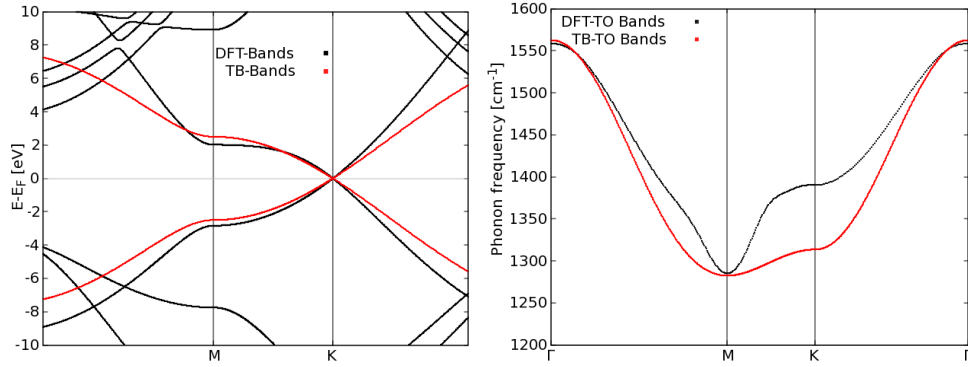In the linear part of the spectrum, where the conduction bands are

FIGURE 3.19: Comparison between the DFT (black) and TB (red) electronic (left) and phonon (right) bands of graphene.
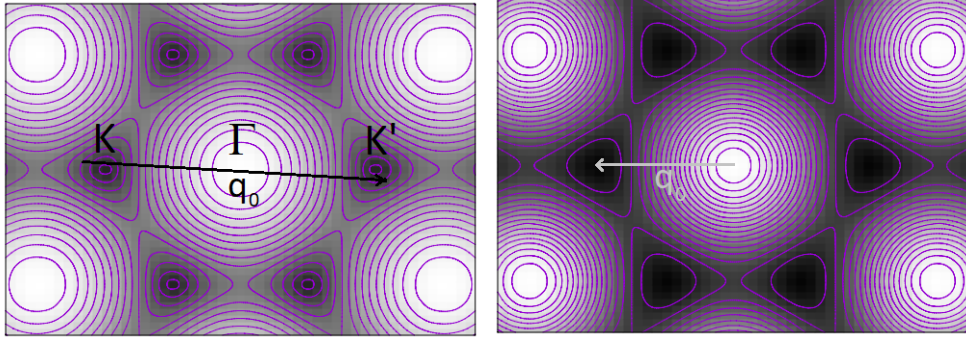

FIGURE 3.20: Inter-valley dispersion of the D mode: allowed $\mathbf{q}$-vector between the K-points, for a Stokes process, from an iso-energetic $E(\mathbf{k}_i)$ to $E(\mathbf{k}_f)$.

approximated by $E(\mathbf{k}) \approx \hbar v_F |\mathbf{k}|$, and $\omega(\mathbf{q}) \approx \omega_0 + \alpha |\mathbf{q}|$, due to the circular symmetry of $\mathbf{q}$ and $\mathbf{k}$, the solutions for q should be identical in either $1D$ or $2D$. However, the Raman line shape must differ in its width in $2D$ due to the surface integration.[154]

As the initial energy exceeds the linear regime, q_0 is no longer a single value. In $1D$, q_0 splits into four possible values, for inter/intra-valley and -band dispersions, as sketched in fig. 3.14 with Raman active modes plotted in fig. 3.15. These modes have been shown to be strongly dependent on the local electronic and phonon properties. Above the linear region, the circular iso-electronic contours around K or K' turn into triangles, the so-called *trigonal warping effect*,[174,180,183] as shown in the left part of fig. 3.21. In this plot I have computed the iso-energetic $\mathbf{k}$-values for different excitation energies ($2E(\mathbf{k})$) around K, and the circular profiles for low energies ($E \sim 2$ eV or below) and the trigonal warping of these bands for higher energies.

The excitation energy of the laser defines the set of $\mathbf{k}_i$ at $E_i = 2E_{Laser}$,

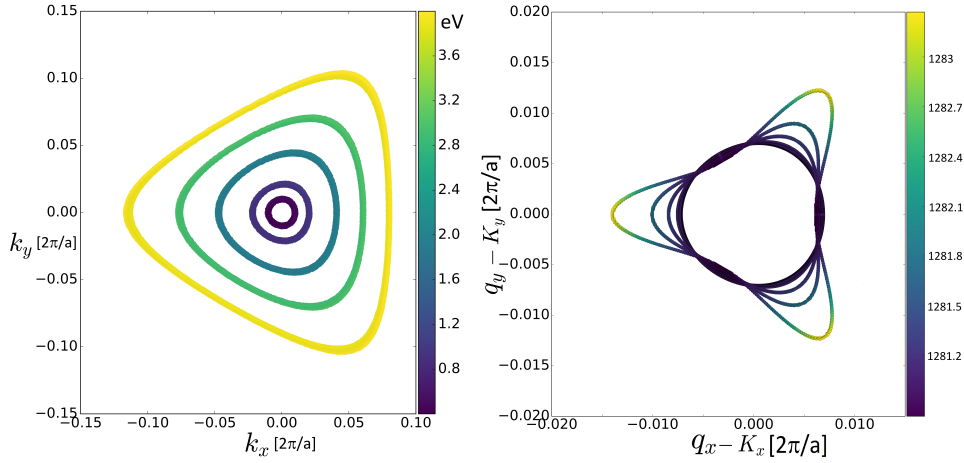**FIGURE 3.21:** Iso-energetic profiles for (left) **k**- and (right) **q**-vectors, for excitation energies of $E = 0.5, 1.0, 2.0, 3.0$ and 4.0 eV. The iso-energetic energy values are presented in each respective color bar.

around the K-point, that are resonantly dispersed to $\mathbf{k}_f$ at E_f around K' by the allowed pairs $(\mathbf{q}_0, \omega)$. I consider the Stokes contributions given by $E_i > E_f$. A set if iso-energetic $\mathbf{k}_i$ vectors for energies between $E_{Laser} = 0.5$ eV and 4.0 eV is shown in the left part of fig. 3.21 and they manifest the local properties of the BZ around the K point.

Now, if I compute the $(\mathbf{q}_0, \omega)$ using solely the conservation of momentum and energy, then I find that all **q** vectors in the phonon surface, below some maximal phonon energy, will match this condition including those vectors lying exactly at K; all kind of intermediate processes are allowed, e.g., all *horizontal* **q** dispersions. By additionally imposing the conservation of the direction of the Fermi velocity, i.e., that the initial and final angle differs by π in **q**-space, the only remaining available **q** modes will lie in the profiles presented in the right part of fig. 3.21. In this plot I present the **q** profiles corresponding to the excitation energies shown in the left part of this figure. I observe, that for low energy values the allowed **q** vectors lie in a circumference, and as the excitation energy increases, this shape is dramatically shifted. Indeed, I observe that there is a minimum and maximum of phonon frequencies for each profile, and that the minimum slightly decreases with increasing the energy. Note also that, as the excitation energy increases, the phonon-frequency range also increases thus showing the Raman dispersion of the D-mode as similarly obtained by the DFT data in fig. 3.15. Therefore, this results indicate that the **q**-surface obtained from conservation rules without restrictions on the normal component are upper-bounded by the **q** line - with varying phonon frequency - obtained by the conservation rules plus

the conservation of the direction of Fermi velocity vector.

Now, I am able to compute the complete Raman profile as function of the excitation energy and the size of the sample, using a modification of eq. (3.6) of the form :

$$I(\omega) \approx \oint\limits_{\mathbf{q}_0} \int \left| C(\mathbf{q}, \mathbf{q}_0) \right|^2 \mathcal{L}(\omega, \omega(\mathbf{q})) d\mathbf{q}, \qquad (3.15)$$

that also considers the contribution, either summation or integration, of the allowed $\mathbf{q}_0$ vectors shown in fig. 3.21. This analysis allows me, in principle, to find differences in 1 and 2D and to directly compare to experiments. However, the mismatch of the phonon and electronic bands, presented in fig. 3.21, precludes this model to have a direct comparison to experiments.

The phonon band structure, as it stands, only considers the Raman shift frequencies in an interval of size ~ 1.8 cm^{-1} for an excitation energy of ~ 4.0 eV. This strong underestimation, since the DFT data indicates a range in the order of 64 cm^{-1}, is caused by the strong mismatch of the phonon bands close to the K-point since DFT data increases more rapidly than the TB bands. However, the non-linear shift of the D-band and the trigonal effects are captured within this simplified approximation without further fits. The $\mathbf{q}$-profiles presented in the right part of fig. 3.21 allow to numerically integrate the complete Raman profile using eq. (3.15). The resulting peak has the equally-weighted contributions of the phonon frequencies corresponding to the allowed range thus defining an extra widening. I trust that, without a numerical-exhaustive integration of fig. 3.21, the TB approach is good enough to observe the energy-dependent position (dispersion) and widening of the peaks. The micro-crystalline behavior is identical as that already observed in fig. 3.16, since the model is in principle system independent, except for integration constants.

3.2.9 Conclusions

In this section I have presented a brief survey of RS phenomena and an introduction to their theoretical treatment. I applied this analysis to the case of graphene to explain the non-dispersive nature of the G-mode and the strongly dispersive D-mode present in the Raman spectra. Using conservation arguments, I found the Raman active q_0-modes and computed the dispersion of the D band that is strongly dependent on the electronic and phonon properties of graphene. The effects of the linear dispersion in graphene, together with an approximate parabolic

phonon TO band at the K-points explains the low-energy (below ~ 2 eV) part of the Raman shift. For larger energies, this unique q_0-value splits either in two points in $1D$, or into a continuous curve in the BZ of $2D$ graphene. The DFT-based numerical trends for the Raman shift of the D-mode show a very good agreement with experimental data, using a $1D$ model. The presence of intermediate data in the peaks is explained by an extension to $2D$ using TB electronic and phonon model bands.

For the model of the Raman peaks, and the effect of finite sizes, I adopted a Lorentzian-like profile with a weight function that depends on the length and allows the transition elements for different q_0-vectors. Within this model, I explain the positive shift observed in the zone-center G mode of about 15 cm^{-1}, as well as the excitation energy-dependent shift of the D-bands. Interestingly, we have found, without a complete physical curiosity, that the experimentally observed allowed **q** vectors must obey, besides the momentum and energy conservation rules, conservation of the Fermi velocity component and therefore the electronic dispersion must lie in the same energy band.

This approximation has not yet been presented in literature, and its importance lies on the fact that I do not have to approximate the bands as linear or constant, but I can consider non-linear effects and fit the experimental data and the TB extension. However, since Raman spectroscopy in carbon is so sensitive to the atomic properties of carbon atoms, purely phenomenological approach will only give some overall properties of the measurements. A complete theoretical model have to account for quantization effects on the electronic bands, the strong dependency on the edges,[184] and a complete solution of the transition probability.

4 Summary and Outline

It is rather difficult to summarize the whole Ph. D. experience in a few words, since it comprehends different aspects of my daily life. My main motivation for such a decision comes from my necessity of increasing my scientific skills, besides getting a different cultural experience. Indeed, this cultural experience is quite away from the scope of the current work, but I may recognize that in fact my work has been strongly influenced by *environmental* factors. Fortunately, I may regard this experience as an enrichment process from variable and unpredictable sources.

An important part of my scientific work is reported in my master thesis and now I can complement my scientific career with the present thesis. I started this research strongly enthusiastic with a panoramic review of the most relevant literature about solid state physics and the approximation methods following the historical development. Of course, I met myself in a big trouble when the list of papers pending for reading exceeded those already read. Then I adopted a more practical review scheme: concentrate in the most (top) relevant literature that will support my forthcoming work.

I received a valuable and considerably intense introduction to the DFT techniques, besides many computational hints, from the already experienced researchers affiliated to the group AG Heiliger. These guidelines allowed me to start my own calculations, from scratch, and to gain a vast experience in the physical properties of materials. It was then just a matter of time to start with the research projects proposed by the researchers in the RTG2204 group.

The project about the electronic properties of thermoelectric Mg_2X materials involved several formal and informal discussions about the scientific interests and the questions that should be addresses. Then I started with the corresponding calculations that accounted very well with the properties already known. However, since I was interested in the electronic properties of alloy systems, I decided to board this problem using the theoretical tools developed in the AG group (KKR-CPA), instead of those conventional in literature (e.g., supercell methods). As it is to be expected, many numerical and physical problems arose that I could circumvent. The solution to these problems now represent a series

of tools in my box to tackle a large variety of computational and physical problems, and most of these are implicitly used in this work but not reported in detail.

This work also received indirect contributions from different discussions held at international conferences, e.g., in Italy or Russia. There, many interested and strongly experienced researchers inquired me about the methods, the results, the interpretation, and many other questions that in any way are out of the scope of my research. This interaction with other researchers allowed me to extend this work to different domains, most of them already reported here, but also many that remain still unexplored or just subject to the judgment of the intuition. It is my hope that many of these questions will be cleared in my future. Nonetheless, in my opinion, the results reported here, provide an important and new source for understanding the electronic and structural features of these intermediate alloys. I can see the projection of this research in future applications, for instance those related to electronic transport, optimization of the thermoelectric performance, evaluation of the thermoelectric efficiency in terms of the atomic features, optimal design of thermoelectric devices, and so further. Hence, I regard this contribution to the scientific community as a fundamental problem, rich of physics, and also nowadays active field in the thermoelectric community.

After not less than one year of starting my Ph. D. training, I drew my attention on a project about Raman spectroscopy in graphene. I already had experience with graphene but with focus on quantum transport in nano-structured materials. The main problem consisted of providing an explanation to the Raman defect-mode existing in nano-structured materials, and its dispersion with the excitation laser energy. I found a plausible description of this phenomena using equilibrium structural and electronic properties, from DFT calculations, and using basic conservation rules from fundamental physics. With this approach, some measurements were readily explained and the theory met the experiments with very good accuracy. Further, conservation rules explained very well a few and important physical quantities that hold in the macroscopic crystalline limit. My attention was then shifted to defect materials, or materials with nano-metric boundaries, in which the rigid Raman signal is deformed. This demanded a Raman peak modeling, and considering a theoretical scheme that accounted for transition probabilities that allow to relax the conservation rules. The phenomenological approach, rather than purely theoretical, resulted very useful and intuitive and allowed me to model not only the graphene systems, but also to extend its application to different systems, e.g., Ce_2O and diamond. Even though this approach

shed a meaningful light about the experimental observations, I still see the possibility of a more complete solution of the problem that not only accounted for the observed shifts but also the intensity decays and the realistic selection rules. This is the case of a physical analysis of the Raman spectroscopy phenomena and the AG Heiliger has an important and deep experience in this kind of calculations.

I think that, after this study of the physical properties of material systems from first-principles methods, I have provided myself with a rich world of new physical concepts and phenomena. This part is relevant for my formation as a researcher since I have developed different several methods. Besides these skills, most of my work has been carried on in a computer and therefore I have learned indispensable numerical and computational tools that allow me to solve problems not only in physics. With this, I mean that I regard this experience, professional and cultural, as an appetizer for a large and promising career as a researcher.

References

[1] W. Kohn, Rev. Mod. Phys. **71**, 1253 (1999) (cit. on pp. 10, 13, 15).

[2] R. G. Parr and W. Yang, *Density-functional theory of atoms and molecules (international series of monographs on chemistry)* (Oxford University Press, USA, 1994) (cit. on p. 10).

[3] J. Kohanoff, *Electronic structure calculations for solids and molecules: theory and computational methods* (Cambridge University Press, 2006) (cit. on pp. 10, 14, 16).

[4] L. H. Thomas, Mathematical Proceedings of the Cambridge Philosophical Society **23**, 542 (1927) (cit. on p. 12).

[5] E. Fermi, Rend. Accad. Naz. Lincei, 6 (1927), pp. 602-607 (1927) (cit. on p. 12).

[6] P. A. M. Dirac, Mathematical Proceedings of the Cambridge Philosophical Society **26**, 376 (1930) (cit. on p. 13).

[7] J. C. Slater, Phys. Rev. **81**, 385 (1951) (cit. on p. 13).

[8] P. Hohenberg and W. Kohn, Phys. Rev. **136**, B864 (1964) (cit. on p. 13).

[9] M. Levy, Phys. Rev. A **26**, 1200 (1982) (cit. on p. 14).

[10] W. Kohn and L. J. Sham, Phys. Rev. **140**, A1133 (1965) (cit. on p. 14).

[11] U. von Barth and L. Hedin, Journal of Physics C: Solid State Physics **5**, 1629 (1972) (cit. on p. 15).

[12] S. H. Vosko, L. Wilk, and M. Nusair, Canadian Journal of Physics **58**, 1200 (1980) (cit. on p. 15).

[13] J. P. Perdew and A. Zunger, Phys. Rev. B **23**, 5048 (1981) (cit. on p. 15).

[14] D. M. Ceperley and B. J. Alder, Phys. Rev. Lett. **45**, 566 (1980) (cit. on p. 15).

[15] D. C. Langreth and M. J. Mehl, Phys. Rev. B **28**, 1809 (1983) (cit. on p. 15).

References

[16] A. D. Becke, Phys. Rev. A **38**, 3098 (1988) (cit. on p. 15).

[17] J. P. Perdew, K. Burke, and M. Ernzerhof, Phys. Rev. Lett. **77**, 3865 (1996) (cit. on pp. 15, 53).

[18] F. Bloch, Zeitschrift für Physik **52**, 555 (1929) (cit. on p. 16).

[19] H. J. Monkhorst and J. D. Pack, Phys. Rev. B **13**, 5188 (1976).

[20] J. M. Ziman, *Principles of the theory of solids*, 2nd ed. (Cambridge University Press, 1972) (cit. on p. 17).

[21] L. Hedin, Phys. Rev. **139**, A796 (1965) (cit. on p. 19).

[22] J. Korringa, Physica **13**, 392 (1947) (cit. on p. 19).

[23] W. Kohn and N. Rostoker, Phys. Rev. **94**, 1111 (1954) (cit. on p. 19).

[24] J. Zabloudil, R. Hammerling, L. Szunyogh, and P. Weinberger, *Electron scattering in solid matter: a theoretical and computational treatise*, Springer Series in Solid-State Sciences (Springer Berlin Heidelberg, 2006) (cit. on p. 20).

[25] M. Czerner, B. Yavorsky, and I. Mertig, physica status solidi (b) **247**, 2594 (2010) (cit. on pp. 21, 29).

[26] L.-W. Wang, L. Bellaiche, S.-H. Wei, and A. Zunger, Phys. Rev. Lett. **80**, 4725 (1998) (cit. on p. 21).

[27] L. Nordheim, Annalen der Physik **401**, 607 (1931) (cit. on p. 21).

[28] L. Bellaiche and D. Vanderbilt, Phys. Rev. B **61**, 7877 (2000) (cit. on p. 21).

[29] P. Soven, Phys. Rev. **156**, 809 (1967) (cit. on pp. 22, 28, 29).

[30] C. Franz, M. Czerner, and C. Heiliger, Phys. Rev. B **88**, 094421 (2013) (cit. on pp. 22, 28, 29).

[31] B. Velický, Phys. Rev. **184**, 614 (1969) (cit. on p. 22).

[32] P. Giannozzi, S. de Gironcoli, P. Pavone, and S. Baroni, Phys. Rev. B **43**, 7231 (1991) (cit. on p. 22).

[33] N. Mounet and N. Marzari, Phys. Rev. B **71**, 205214 (2005) (cit. on pp. 23, 24).

[34] H. Hellmann, *Einfuhring in die quantemchemie* (J.W. Edwards in Ann Arbor, Mich, 1944) (cit. on p. 23).

[35] R. P. Feynman, Phys. Rev. **56**, 340 (1939) (cit. on p. 23).

[36] P. Pavone, K. Karch, O. Schütt, D. Strauch, W. Windl, P. Giannozzi, and S. Baroni, Phys. Rev. B **48**, 3156 (1993) (cit. on p. 24).

[37] F. D. Murnaghan, Proceedings of the National Academy of Sciences **30**, 244 (1944) (cit. on p. 24).

[38] F. Birch, Phys. Rev. **71**, 809 (1947) (cit. on p. 24).

[39] S. Baroni, S. de Gironcoli, A. Dal Corso, and P. Giannozzi, Rev. Mod. Phys. **73**, 515 (2001) (cit. on p. 24).

[40] D. Rowe, *Crc handbook of thermoelectrics* (CRC-Press, 1995) (cit. on pp. 26, 27, 29, 32, 39).

[41] E. N. Nikitin, V. G. Bazanov, and T. V. I., Sov. Phys. Sol. State **3**, 2648 (1961) (cit. on pp. 26, 37).

[42] R. J. LaBotz, D. R. Mason, and D. F. O'kane, J. Electrochem. Soc. **110**, 127 (1963) (cit. on pp. 26, 27, 33, 37–39).

[43] M. I. Fedorov, V. K. Zaitsev, and G. N. Isachenko, in Solid compounds of transition elements, Vol. 170, Solid State Phenomena (Mar. 2011), pp. 286–292 (cit. on pp. 27, 37, 39).

[44] V. K. Zaitsev, M. I. Fedorov, E. A. Gurieva, I. S. Eremin, P. P. Konstantinov, A. Y. Samunin, and M. V. Vedernikov, Phys. Rev. B **74**, 045207 (2006) (cit. on pp. 27, 28, 39).

[45] D. D. Hsu, *Chemicool periodic table*, (2018) (cit. on p. 27).

[46] J. A. Ober, *Mineral commodity summaries* (U.S. Geological Survey, 2018) (cit. on p. 27).

[47] U. Winkler, Helv. Phys. Acta **28**, 633 (1955) (cit. on pp. 27, 28, 37, 39).

[48] R. G. Morris, R. D. Redin, and G. C. Danielson, Phys. Rev. **109**, 1909 (1958) (cit. on pp. 27, 28, 37, 39).

[49] R. D. Redin, R. G. Morris, and G. C. Danielson, Phys. Rev. **109**, 1916 (1958) (cit. on pp. 27, 28, 39).

[50] C. A. Mead, Journal of Applied Physics **35**, 2460 (1964) (cit. on pp. 27, 28).

[51] R. F. Blunt, H. P. R. Frederikse, and W. R. Hosler, Phys. Rev. **100**, 663 (1955) (cit. on pp. 27, 28).

[52] F. Vazquez, R. A. Forman, and M. Cardona, Phys. Rev. **176**, 905 (1968) (cit. on pp. 27, 28, 39).

[53] A. Stella, A. D. Brothers, R. H. Hopkins, and D. W. Lynch, physica status solidi (b) **23**, 697 (1967) (cit. on pp. 27, 39).

[54] L. A. Lott and D. W. Lynch, Phys. Rev. **141**, 681 (1966) (cit. on pp. 27, 28, 39).

References

[55] H. G. Lipson and A. Kahan, Phys. Rev. **133**, A800 (1964) (cit. on pp. 27, 28).

[56] W. J. Scouler, Phys. Rev. **178**, 1353 (1969) (cit. on pp. 27, 38, 39).

[57] P. Koenig, D. Lynch, and G. Danielson, Journal of Physics and Chemistry of Solids **20**, 122 (1961) (cit. on p. 27).

[58] M. Heller and G. Danielson, J. Phys. Chem. Sol. **23**, 265 (1962) (cit. on pp. 27, 28, 39).

[59] J. E. Mahan, A. Vantomme, G. Langouche, and J. P. Becker, Phys. Rev. B **54**, 16965 (1996) (cit. on pp. 27, 39).

[60] W. D. Robertson and H. H. Uhlig, Trans. Am. Inst. Mining Met. Engrs. **180**, 345 (1949) (cit. on p. 27).

[61] T. M. Tritt, Science **272**, 1276 (1996) (cit. on p. 27).

[62] Y. Pei, H. Wang, and G. J. Snyder, Advanced Materials **24**, 6125 (2012) (cit. on pp. 27, 28, 40).

[63] Q. Zhang, J. He, T. J. Zhu, S. N. Zhang, X. B. Zhao, and T. M. Tritt, Applied Physics Letters **93**, 102109 (2008) (cit. on p. 27).

[64] J. L. Corkill and M. L. Cohen, Phys. Rev. B **48**, 17138 (1993) (cit. on pp. 27, 37, 39).

[65] P. M. Lee, Phys. Rev. **135**, A1110 (1964) (cit. on pp. 27, 28, 30, 38, 39).

[66] D. M. Wood and A. Zunger, Phys. Rev. B **34**, 4105 (1986) (cit. on pp. 27–30, 37).

[67] M. Y. Au-Yang and M. L. Cohen, Phys. Rev. **178**, 1358 (1969) (cit. on pp. 27, 28, 30, 38, 39).

[68] J. Tejeda and M. Cardona, Phys. Rev. B **14**, 2559 (1976) (cit. on p. 27).

[69] F. Aymerich and G. Mula, physica status solidi (b) **42**, 697 (1970) (cit. on pp. 27, 38, 39).

[70] K. Huebner, Physica Status Solidi (b) **64**, K55 (1974) (cit. on pp. 27, 39).

[71] G. H. Grosch and K.-J. Range, Journal of Alloys and Compounds **235**, 250 (1996) (cit. on pp. 27, 28, 33, 37).

[72] B. Arnaud and M. Alouani, Phys. Rev. B **64**, 033202 (2001) (cit. on pp. 27–29, 34, 38, 39).

[73] J. Bourgeois, J. Tobola, B. Wiendlocha, L. Chaput, P. Zwolenski, D. Berthebaud, F. Gascoin, Q. Recour, and H. Scherrer, Functional Materials Letters **06**, 1340005 (2013) (cit. on pp. 27–29, 33, 37, 39, 41).

[74] H. Wang, W. Chu, and H. Jin, Computational Materials Science **60**, 224 (2012) (cit. on p. 27).

[75] H. Mizoguchi, Y. Muraba, D. C. Fredrickson, S. Matsuishi, T. Kamiya, and H. Hosono, Angewandte Chemie International Edition **56**, 10135 (2017) (cit. on pp. 27, 33).

[76] K. Kutorasinski, B. Wiendlocha, J. Tobola, and S. Kaprzyk, Phys. Rev. B **89**, 115205 (2014) (cit. on pp. 27, 29, 34).

[77] V. Zaitsev, E. Nikitin, and E. Tkalenko, Soviet Physics of Solid State **11**, 3000 (1969) (cit. on pp. 27, 39).

[78] J. de Boor, U. Saparamadu, J. Mao, K. Dahal, E. Mueller, and Z. Ren, Acta Materialia **120**, 273 (2016) (cit. on p. 27).

[79] G. N. Isachenko, V. K. Zaitsev, M. I. Fedorov, A. T. Burkov, E. A. Gurieva, P. P. Konstantinov, and M. V. Vedernikov, Physics of the Solid State **51**, 1796 (2009) (cit. on p. 27).

[80] R. Viennois, P. Jund, C. Colinet, and J.-C. Tédenac, Journal of Solid State Chemistry **193**, Solid State Chemistry and Materials Science of Thermoelectric Materials, 133 (2012) (cit. on pp. 27, 32, 33, 39, 44).

[81] Y. Noda, H. Kon, Y. Furukawa, I. A. Nishida, and K. Masumoto, Materials Transactions, JIM **33**, 851 (1992) (cit. on pp. 27, 38, 39).

[82] M. Akasaka, T. Iida, K. Nishio, and Y. Takanashi, Thin Solid Films **515**, APAC-SILICIDE 2006, 8237 (2007) (cit. on pp. 27, 39).

[83] E. Ratai, M. P. Augustine, and S. M. Kauzlarich, The Journal of Physical Chemistry B **107**, 12573 (2003) (cit. on p. 27).

[84] L. Vegard, Zeitschrift für Physik **5**, 17 (1921) (cit. on pp. 27, 36).

[85] K. Kutorasiski, J. Tobola, and S. Kaprzyk, Phys. Rev. B **87**, 195205 (2013) (cit. on pp. 28, 29, 36, 39).

References

[86] V. K. Zaitsev, G. N. Isachenko, and A. T. Burkov, "Efficient thermoelectric materials based on solid solutions of mg2x compounds (x = si, ge, sn)", in *Thermoelectrics for power generation - a look at trends in the technology*, edited by S. Skipidarov and M. Nikitin (InTech, Rijeka, 2016) Chap. 11 (cit. on pp. 27, 39).

[87] R. Song, T. Aizawa, and J. Sun, Materials Science and Engineering: B **136**, 111 (2007) (cit. on pp. 27, 37).

[88] Y. Isoda, T. Nagai, H. Fujiu, Y. Imai, and Y. Shinohara, in 2006 25th international conference on thermoelectrics (Aug. 2006), pp. 406–410 (cit. on p. 27).

[89] Y. Pei, X. Shi, A. LaLonde, H. Wang, L. Chen, and G. J. Snyder, Nature **473**, 66 (2011) (cit. on pp. 27, 36).

[90] W. Liu, X. Tan, K. Yin, H. Liu, X. Tang, J. Shi, Q. Zhang, and C. Uher, Phys. Rev. Lett. **108**, 166601 (2012) (cit. on pp. 27, 37, 39, 43).

[91] W. Li, L. Lindsay, D. A. Broido, D. A. Stewart, and N. Mingo, Phys. Rev. B **86**, 174307 (2012) (cit. on pp. 27, 30).

[92] W. Luo, M. Yang, F. Chen, Q. Shen, H. Jiang, and L. Zhang, Materials Science and Engineering: B **157**, 96 (2009) (cit. on pp. 27, 37, 39).

[93] P. Boulet, M. Verstraete, J.-P. Crocombette, M. Briki, and M.-C. Record, Computational Materials Science **50**, 847 (2011) (cit. on pp. 27, 29, 33, 39).

[94] M. Fedorov, E. Gurieva, I. Eremin, P. Konstantinov, A. Y. Samunin, V. Zaitsev, S. Sano, and L. Rauscher, 2nd Europ. Conf. on Thermoelectrics **2**, 72 (2004) (cit. on p. 27).

[95] M. I. Fedorov, V. K. Zaitsev, G. N. Isachenko, I. S. Eremin, E. A. Gurieva, A. T. Burkov, P. P. Konstantinov, and A. A. Shabaldin, in Ict 2005. 24th international conference on thermoelectrics, 2005. (June 2005), pp. 110–113 (cit. on pp. 28, 39).

[96] G. S. Nolas, D. Wang, and M. Beekman, Phys. Rev. B **76**, 235204 (2007) (cit. on p. 28).

[97] J. Tobola, S. Kaprzyk, and H. Scherrer, Journal of Electronic Materials **39**, 2064 (2010) (cit. on p. 28).

[98] S. Kim, B. Wiendlocha, H. Jin, J. Tobola, and J. P. Heremans, Journal of Applied Physics **116**, 153706 (2014) (cit. on p. 28).

[99] L. Zhang, P. Xiao, L. Shi, G. Henkelman, J. B. Goodenough, and J. Zhou, Journal of Applied Physics **117**, 155103 (2015) (cit. on pp. 28, 33, 37, 39).

[100] T. Dasgupta, C. Stiewe, R. Hassdorf, A. J. Zhou, L. Boettcher, and E. Mueller, Phys. Rev. B **83**, 235207 (2011) (cit. on p. 28).

[101] A. Kato, T. Yagi, and N. Fukusako, Journal of Physics: Condensed Matter **21**, 205801 (2009) (cit. on p. 28).

[102] P. Jund, R. Viennois, C. Colinet, G. Hug, M. Fèvre, and J.-C. Tédenac, Journal of Physics: Condensed Matter **25** (2013) (cit. on pp. 28, 37, 39).

[103] G. Jiang, J. He, T. Zhu, C. Fu, X. Liu, L. Hu, and X. Zhao, Advanced Functional Materials **24**, 3776 (2014) (cit. on p. 28).

[104] P. Zwolenski, J. Tobola, and S. Kaprzyk, Journal of Electronic Materials **40**, 889 (2011) (cit. on pp. 28, 31, 33, 43).

[105] X. Liu, L. Xi, W. Qiu, J. Yang, T. Zhu, X. Zhao, and W. Zhang, Advanced Electronic Materials **2**, 1500284, 1500284 (2016) (cit. on p. 28).

[106] N. Hirayama, T. Iida, K. Nishio, Y. Kogo, K. Takarabe, and N. Hamada, Japanese Journal of Applied Physics **56**, 05DC05 (2017) (cit. on p. 28).

[107] N. Hirayama, T. Iida, S. Morioka, M. Sakamoto, K. Nishio, Y. Kogo, Y. Takanashi, and N. Hamada, Journal of Materials Research **30**, 2564 (2015) (cit. on pp. 28, 33).

[108] M. Søndergaard, M. Christensen, K. A. Borup, H. Yin, and B. Iversen, Journal of Electronic Materials **42**, 1417 (2013) (cit. on p. 28).

[109] J. Mao, H. S. Kim, J. Shuai, Z. Liu, R. He, U. Saparamadu, F. Tian, W. Liu, and Z. Ren, Acta Materialia **103**, 633 (2016) (cit. on p. 28).

[110] X. Liu, T. Zhu, H. Wang, L. Hu, H. Xie, G. Jiang, G. J. Snyder, and X. Zhao, Advanced Energy Materials **3**, 1238 (2013) (cit. on pp. 28, 43).

[111] W. Liu, X. Tang, and J. Sharp, Journal of Physics D: Applied Physics **43**, 085406 (2010) (cit. on p. 28).

References

[112] W. Liu, H. S. Kim, S. Chen, Q. Jie, B. Lv, M. Yao, Z. Ren, C. P. Opeil, S. Wilson, C.-W. Chu, and Z. Ren, Proceedings of the National Academy of Sciences **112**, 3269 (2015) (cit. on pp. 28, 37).

[113] H. Ihou-Mouko, C. Mercier, J. Tobola, G. Pont, and H. Scherrer, Journal of Alloys and Compounds **509**, 6503 (2011) (cit. on pp. 28, 36).

[114] J. J. Pulikkotil, D. J. Singh, S. Auluck, M. Saravanan, D. K. Misra, A. Dhar, and R. C. Budhani, Phys. Rev. B **86**, 155204 (2012) (cit. on pp. 28–30, 33, 36, 37, 39).

[115] X. J. Tan, W. Liu, H. J. Liu, J. Shi, X. F. Tang, and C. Uher, Phys. Rev. B **85**, 205212 (2012) (cit. on pp. 28, 33, 37, 39).

[116] J. Sun and D. J. Singh, Phys. Rev. Applied **5**, 024006 (2016) (cit. on pp. 28, 29).

[117] K.-y. Li, Y. Lu, Y. Huang, and X.-h. Shao, Chinese Physics B **26**, 066103 (2017) (cit. on p. 28).

[118] S. Bhattacharya and G. K. H. Madsen, Phys. Rev. B **92**, 085205 (2015) (cit. on p. 28).

[119] J. J. Pulikkotil, H. N. Alshareef, and U. Schwingenschlögl, Journal of Physics: Condensed Matter **22**, 352204 (2010) (cit. on pp. 28, 31, 37, 38).

[120] W. Liu, H. Chi, H. Sun, Q. Zhang, K. Yin, X. Tang, Q. Zhang, and C. Uher, Phys. Chem. Chem. Phys. **16**, 6893 (2014) (cit. on pp. 28, 36, 41, 43).

[121] T. Dasgupta, C. Stiewe, J. de Boor, and E. Müller, physica status solidi (a) **211**, 1250 (2014) (cit. on p. 28).

[122] J. S. Faulkner and G. M. Stocks, Phys. Rev. B **21**, 3222 (1980) (cit. on p. 29).

[123] O. Gunnarsson and B. I. Lundqvist, Phys. Rev. B **13**, 4274 (1976) (cit. on p. 29).

[124] N. O. Folland, Phys. Rev. **158**, 764 (1967) (cit. on pp. 30, 33, 39).

[125] J.-i. Tani and H. Kido, Intermetallics **15**, 1202 (2007) (cit. on p. 31).

[126] R. Viennois, C. Colinet, P. Jund, and J.-C. Tédenac, Intermetallics **31**, 145 (2012) (cit. on pp. 31, 32).

[127] G.-X. Qian, R. M. Martin, and D. J. Chadi, Phys. Rev. B **38**, 7649 (1988) (cit. on p. 31).

[128] S. B. Zhang and J. E. Northrup, Phys. Rev. Lett. **67**, 2339 (1991) (cit. on p. 31).

[129] A. Kozlov, J. Gröbner, and R. Schmid-Fetzer, Journal of Alloys and Compounds **509**, 3326 (2011) (cit. on p. 32).

[130] I.-H. Jung and J. Kim, Journal of Alloys and Compounds **494**, 137 (2010) (cit. on p. 32).

[131] I.-H. Jung, D.-H. Kang, W.-J. Park, N. J. Kim, and S. Ahn, Calphad **31**, 192 (2007) (cit. on p. 32).

[132] A. R. Oganov and C. W. Glass, The Journal of Chemical Physics **124**, 244704 (2006) (cit. on p. 33).

[133] Q. Zhang, X. B. Zhao, T. J. Zhu, and J. P. Tu, physica status solidi (RRL) – Rapid Research Letters **2**, 56 (2008) (cit. on p. 33).

[134] K. Mars, H. Ihou-Mouko, G. Pont, J. Tobola, and H. Scherrer, Journal of Electronic Materials **38**, 1360 (2009) (cit. on p. 33).

[135] R. O. Jones and O. Gunnarsson, Rev. Mod. Phys. **61**, 689 (1989) (cit. on p. 33).

[136] W. Fan, R. Chen, L. Wang, P. Han, and Q. Meng, Journal of Electronic Materials **40**, 1209 (2011) (cit. on p. 33).

[137] H. Ebert, D. Ködderitzsch, and J. Minár, Reports on Progress in Physics **74**, 096501 (2011) (cit. on p. 36).

[138] N. Satyala and D. Vashaee, Applied Physics Letters **100**, 073107 (2012) (cit. on pp. 36, 40).

[139] P. Gao, I. Berkun, R. D. Schmidt, M. F. Luzenski, X. Lu, P. Bordon Sarac, E. D. Case, and T. P. Hogan, Journal of Electronic Materials **43**, 1790 (2014) (cit. on p. 36).

[140] W. Liu, X. Tang, H. Li, J. Sharp, X. Zhou, and C. Uher, Chemistry of Materials **23**, 5256 (2011) (cit. on p. 36).

[141] H. Wang, A. D. LaLonde, Y. Pei, and G. J. Snyder, Advanced Functional Materials **23**, 1586 (2013) (cit. on p. 36).

[142] D. J. Singh and I. I. Mazin, Phys. Rev. B **56**, R1650 (1997) (cit. on p. 36).

[143] Z. Du, T. Zhu, Y. Chen, J. He, H. Gao, G. Jiang, T. M. Tritt, and X. Zhao, J. Mater. Chem. **22**, 6838 (2012) (cit. on p. 36).

[144] R. Janot, F. Cuevas, M. Latroche, and A. Percheron-Guégan, Intermetallics **14**, 163 (2006) (cit. on p. 37).

[145] O. Benhelal, A. Chahed, S. Laksari, B. Abbar, B. Bouhafs, and H. Aourag, physica status solidi (b) **242**, 2022 (2005) (cit. on pp. 37, 39).

[146] G. Jiang, L. Chen, J. He, H. Gao, Z. Du, X. Zhao, T. M. Tritt, and T. Zhu, Intermetallics **32**, 312 (2013) (cit. on pp. 37, 39).

[147] P. Baranek and J. Schamps, The Journal of Physical Chemistry B **103**, 2601 (1999) (cit. on pp. 38, 39).

[148] J.-H. Bahk, Z. Bian, and A. Shakouri, Phys. Rev. B **89**, 075204 (2014) (cit. on p. 39).

[149] M. I. Fedorov, D. A. Pshenay-Severin, V. K. Zaitsev, S. Sano, and M. V. Vedernikov, in Thermoelectrics, 2003 twenty-second international conference on - ict (Aug. 2003), pp. 142–145 (cit. on p. 39).

[150] A. Smekal, Naturwissenschaften **11**, 873 (1923) (cit. on p. 45).

[151] C. V. Raman and K. S. Krishnan, Nature **121**, 501 (1928) (cit. on p. 45).

[152] R. M. Martin and L. M. Falicov, "Resonant raman scattering", in *Light scattering in solids*, edited by M. Cardona (Springer Berlin Heidelberg, Berlin, Heidelberg, 1975), pp. 79–145 (cit. on pp. 45–47).

[153] P. Y. Yu and M. Cardona, *Fundamentals of Semiconductors: Physics and Materials Properties* (Springer, Berlin, 2005) (cit. on p. 46).

[154] J. Maultzsch, S. Reich, and C. Thomsen, Phys. Rev. B **70**, 155403 (2004) (cit. on pp. 47, 52, 57, 62).

[155] H. Richter, Z. Wang, and L. Ley, Solid State Communications **39**, 625 (1981) (cit. on p. 48).

[156] I. Campbell and P. Fauchet, Solid State Communications **58**, 739 (1986) (cit. on p. 48).

[157] V. Zólyomi and J. Kürti, Phys. Rev. B **66**, 073418 (2002) (cit. on pp. 50, 57).

[158] A. H. Castro Neto, F. Guinea, N. M. R. Peres, K. S. Novoselov, and A. K. Geim, Rev. Mod. Phys. **81**, 109 (2009) (cit. on pp. 50, 51, 53, 56, 61).

[159] M. J. Matthews, M. A. Pimenta, G. Dresselhaus, M. S. Dresselhaus, and M. Endo, Phys. Rev. B **59**, R6585 (1999) (cit. on pp. 50, 51, 57).

[160] F. Tuinstra and J. L. Koenig, The Journal of Chemical Physics **53**, 1126 (1970) (cit. on pp. 50, 52, 61).

[161] A. Ferrari, J. Robertson, S. Reich, and C. Thomsen, Philosophical Transactions of the Royal Society of London. Series A: Mathematical, Physical and Engineering Sciences **362**, 2271 (2004) (cit. on pp. 51, 52).

[162] D. M. Basko, New Journal of Physics **11**, 095011 (2009) (cit. on p. 51).

[163] Y. Wang, D. C. Alsmeyer, and R. L. McCreery, Chemistry of Materials **2**, 557 (1990) (cit. on pp. 52, 57).

[164] R. Vidano, D. Fischbach, L. Willis, and T. Loehr, Solid State Communications **39**, 341 (1981) (cit. on p. 52).

[165] I. Pócsik, M. Hundhausen, M. Koós, and L. Ley, Journal of Non-Crystalline Solids **227-230**, 1083 (1998) (cit. on pp. 52, 57, 59).

[166] J. Kürti, V. Zólyomi, A. Grüneis, and H. Kuzmany, Phys. Rev. B **65**, 165433 (2002) (cit. on p. 52).

[167] C. Thomsen and S. Reich, Phys. Rev. Lett. **85**, 5214 (2000) (cit. on pp. 52, 57).

[168] J. Maultzsch, S. Reich, and C. Thomsen, Phys. Rev. B **64**, 121407 (2001) (cit. on p. 52).

[169] D. M. Basko, Phys. Rev. B **78**, 125418 (2008) (cit. on p. 52).

[170] P. Giannozzi, S. Baroni, N. Bonini, M. Calandra, R. Car, C. Cavazzoni, D. Ceresoli, G. L. Chiarotti, M. Cococcioni, I. Dabo, A. D. Corso, S. de Gironcoli, S. Fabris, G. Fratesi, R. Gebauer, U. Gerstmann, C. Gougoussis, A. Kokalj, M. Lazzeri, L. Martin-Samos, N. Marzari, F. Mauri, R. Mazzarello, S. Paolini, A. Pasquarello, L. Paulatto, C. Sbraccia, S. Scandolo, G. Sclauzero, A. P. Seitsonen, A. Smogunov, P. Umari, and R. M. Wentzcovitch, Journal of Physics: Condensed Matter **21**, 395502 (2009) (cit. on p. 52).

[171] P. Giannozzi, O. Andreussi, T. Brumme, O. Bunau, M. B. Nardelli, M. Calandra, R. Car, C. Cavazzoni, D. Ceresoli, M. Cococcioni, N. Colonna, I. Carnimeo, A. D. Corso, S. de Gironcoli, P. Delugas, R. A. DiStasio, A. Ferretti, A. Floris, G. Fratesi, G. Fugallo, R. Gebauer, U. Gerstmann, F. Giustino, T. Gorni, J. Jia, M. Kawamura, H.-Y. Ko, A. Kokalj, E. Küçükbenli, M. Lazzeri, M. Marsili, N. Marzari, F. Mauri, N. L. Nguyen, H.-V. Nguyen,

A. Otero-de-la-Roza, L. Paulatto, S. Poncé, D. Rocca, R. Sabatini, B. Santra, M. Schlipf, A. P. Seitsonen, A. Smogunov, I. Timrov, T. Thonhauser, P. Umari, N. Vast, X. Wu, and S. Baroni, Journal of Physics: Condensed Matter **29**, 465901 (2017) (cit. on p. 52).

[172] W. Li, G. Cheng, Y. Liang, B. Tian, X. Liang, L. Peng, A. H. Walker, D. J. Gundlach, and N. V. Nguyen, Carbon **99**, 348 (2016) (cit. on p. 53).

[173] P. R. Wallace, Phys. Rev. **71**, 622 (1947) (cit. on pp. 53, 61).

[174] R. Saito, A. Jorio, A. G. Souza Filho, G. Dresselhaus, M. S. Dresselhaus, and M. A. Pimenta, Phys. Rev. Lett. **88**, 027401 (2001) (cit. on pp. 53, 55, 62).

[175] J. Maultzsch, S. Reich, C. Thomsen, H. Requardt, and P. Ordejón, Phys. Rev. Lett. **92**, 075501 (2004) (cit. on pp. 53, 54).

[176] M. Mohr, J. Maultzsch, Dobard ži ć, S. Reich, Milo ševi ć, Damnjanovi ć, A. Bosak, M. Krisch, and C. Thomsen, Phys. Rev. B **76**, 035439 (2007) (cit. on pp. 53, 54).

[177] S. Piscanec, M. Lazzeri, F. Mauri, A. C. Ferrari, and J. Robertson, Phys. Rev. Lett. **93**, 185503 (2004) (cit. on p. 54).

[178] L. Malard, M. Pimenta, G. Dresselhaus, and M. Dresselhaus, Physics Reports **473**, 51 (2009) (cit. on p. 55).

[179] P. Tan, Y. Deng, and Q. Zhao, Phys. Rev. B **58**, 5435 (1998) (cit. on p. 57).

[180] L. G. Cancado, M. A. Pimenta, R. Saito, A. Jorio, L. O. Ladeira, A. Grueneis, A. G. Souza-Filho, G. Dresselhaus, and M. S. Dresselhaus, Phys. Rev. B **66**, 035415 (2002) (cit. on pp. 58, 62).

[181] D. S. Knight and W. B. White, Journal of Materials Research **4**, 385 (1989) (cit. on p. 61).

[182] M. Lucchese, F. Stavale, E. M. Ferreira, C. Vilani, M. Moutinho, R. B. Capaz, C. Achete, and A. Jorio, Carbon **48**, 1592 (2010) (cit. on p. 61).

[183] P. Venezuela, M. Lazzeri, and F. Mauri, Phys. Rev. B **84**, 035433 (2011) (cit. on p. 62).

[184] L. Brey and H. A. Fertig, Phys. Rev. B **73**, 235411 (2006) (cit. on p. 65).

List of publications

During the course of the Ph. D. position, one publication has been accepted, and some others are still in preparation

[E1] Juan M. Guerra, Carsten Mahr, Marcel Giar, Michael Czerner, and Christian Heiliger, *Ab initio calculations of electronic band structure and effective-mass parameters of thermoelectric $Mg_2X_{1-x}Y_x$ (X, Y=Si, Ge, or Sn) pseudobinary alloys*. Phys. Rev. Materials, **2** 104605 (2018).

[E2] Juan M. Guerra, Carsten Mahr, Marcel Giar, Michael Czerner, and Christian Heiliger, *Ab initio calculations of conduction band effective mass parameters of thermoelectric $Mg_2X_{1-x}Y_x$ (X, Y=Si, Ge, Sn) alloys*. (In preparation)

[E3] Dominique B. Schüpfer, Felix Badaczewski, Juan M. Guerra, Detlev M. Hoffmann, Christian Heiliger, and Peter J. Klar. *Classification and structural description of carbons via Raman spectroscopy*. (In preparation)

[E4] Elifkübra Özkan, Bernd M. Smarsly, Martin Votsmeier, Alexander Hofmann, Felix Benfer, Juan M. Guerra, and Christian Heiliger. *Controlled synthesis and characterization of cerium oxide nanoparticles with different particle sizes*. Journal of Phys. Chem. C (In preparation)

[E5] Further calculations are still pending to be published: anti-Stokes Raman spectra in graphene, and Raman spectra in micro-crystalline diamond.

Conferences and posters

During my Ph. D. training, the RTG2204 supported the participation in the following events:

1. Conference: What about U? - Effects of Hubbard Interactions and Hund's Coupling in Solids | smr 2827 | 17.10-21.10 2016, in Triest, Italy. Participation only.

2. DPG Spring Meeting of the Condensed Matter Section (SKM) | 19.03-24.03 2017, in Dresden, Germany. Poster: Electronic properties of the thermoelectric Mg_2X (X = Si, Ge, Sn)-based alloys.

3. 15th European Conference on Thermoeletrics (ECT2017) | 25.09-27.09 2017, in Padua, Italy. Talk: Electronic and transport properties of the thermoelectric $Mg_2X_{1-x}Sn_x$ (X = Si, Ge, and $0 \leq x \leq 1$)-alloys.

4. DPG Spring Meeting of the Condensed Matter Section (SKM) | 11.03-16.03 2018 in Berlin, Germany. Talk: Electronic and transport properties of the thermoelectric Mg_2X (X = Si, Ge, Sn) substitutional alloys.

5. XI Interstate Conference "Thermoelectrics and their Application" (ISCTA2018) | 08.10-12.10 2018 in St. Petersburg, Russia. Talk: *ab-initio* calculations of electronic band structures and effective-mass parameters of thermoelectric $Mg_2X_{1-x}Y_x$ (X, Y = Si, Ge, Sn) pseudo-binary alloys.

6. 19th International Workshop on Computational Physics and Material Science: Total Energy and Force Methods | (smr 3266) | 09.01-11.01 2019, in Triest, Italy. (Participation only)

7. Workshop on Crystal Structure Prediction: Exploring the Mendeleev Table as a Palette to Design New Materials | (smr 3267) | 14.01 - 18.01 2019, in Triest, Italy. Poster: Ab-initio Structural, Electronic Band Structure and Effective Mass Parameters of Thermoelectric $Mg_2X_{1-x}Y_x$ (X, Y = Si, Ge, Sn) Alloys.

References

8. DPG Spring Meeting of the Condensed Matter Section (SKM) | 31.03-05.04 2019, in Regensburg, Germany. Poster: Ab-initio Structural, Electronic Band Structure and Effective Mass Parameters of Thermoelectric $Mg_2X_{1-x}Y_x$ (X, Y = Si, Ge, Sn) Alloys.

Acknowledgements

References

the world, mainly in South America. I dedicate this work to them. This experience has left not only solid concepts about the scientific world but also an incommensurate love: Simchen, thank you for everything and more.

Eidesstattliche Erklärung

Ich erkläre:

Ich habe die vorgelegte Dissertation selbständig und ohne unerlaubte fremde Hilfe und nur mit den Hilfen angefertigt, die ich in der Dissertation angegeben habe. Alle Textstellen, die wörtlich ider sinngemäß aus veröffentlichten Schriften entnommen sind, und alle Angaben, die auf mündlichen Auskünften beruhen, sind als solche kenntlich gemacht. Bei den von mir durchgeführten und in der Dissertation erwähnten Untersuchungen habe ich die Grundsätze guter wissenschaftlicher Praxis, wie sie in der Satzung der Justus-Liebig-Universität Gießen zur Sicherung guter wissenschaftlicher Praxis niedergelegt sind, eingehalten.

Juan M. Guerra